UNIVERSIDADE DE SÃO PAULO
ESCOLA POLITÉCNICA
DEPARTAMENTO DE ENGENHARIA MECÂNICA

GIOVANI HIDALGO CEOTTO
GUILHERME CASTRIGNANO TAVARES

Injector and combustion chamber design for a nitrous oxide and ethanol rocket engine

São Paulo
2020

UNIVERSIDADE DE SÃO PAULO
ESCOLA POLITÉCNICA
DEPARTAMENTO DE ENGENHARIA MECÂNICA

GIOVANI HIDALGO CEOTTO
GUILHERME CASTRIGNANO TAVARES

Injector and combustion chamber design for a nitrous oxide and ethanol rocket enginel

Trabalho de formatura apresentado à Escola Politécnica da Universidade de São Paulo para obtenção do título de Engenheiro Mecânico.

Área de concentração: Engenharia Mecânica

Orientador: Prof. Dr. Guenther Carlos Krieger Filho

São Paulo
2020

Catalogação-na-publicação

Ceotto, Giovani
Injector and combustion chamber design for a nitrous oxide and ethanolrocket engine / G. Ceotto, G. Tavares -- São Paulo, 2020.
94 p.

Trabalho de Formatura - Escola Politécnica da Universidade de São Paulo. Departamento de Engenharia Mecânica.

1.FOGUETES COM COMBUSTÍVEL LÍQUIDO 2.INJEÇÃO (ENGENHARIA) 3.COMBUSTÃO 4.ACÚSTICA 5.COMBUSTÍVEIS LÍQUIDOS I.Universidade de São Paulo. Escola Politécnica. Departamento de Engenharia Mecânica II.t. III.Tavares, Guilherme

ABSTRACT

This report presents the basic design of a rocket engine injector and combustion chamber for saturated nitrous oxide and liquid ethanol, as well as details of the construction and operation of the engine in which the injectors will be used. At first, an oxidant-fuel mixture is selected based on a thermochemical analysis that explores several existing options and other combinations that have not yet been studied. As a result, nitrous oxide is chosen as an oxidant and ethanol as fuel. Then a simplified methodology is proposed for the design of a pressure-swirl injector responsible for ethanol. Computational fluid dynamics is used to verify the validity of the above-mentioned analysis, using Volume of Fluid (VOF). For the nitrous oxide injector, the flash-boiling phenomenon is investigated, verifying its importance for the ongoing project. The effect is treated analytically using the Dyer model to account for non-equilibrium thermodynamics. Simplified zero-dimensional and one-dimensional combustion models are explored as tools to design the rocket combustion chamber. Furthermore, combustion instability due to acoustic phenomena is studied, with the first spinning tangential mode being computed for the herein developed motor and an ensemble of acoustic cavities being developed to suppress the aforementioned mode. Finally, a preliminary diagram of the static test bench which will be used to validate the injectors and the designed engine is also presented.

Keywords: Liquid rocket motor. Injector. Pressure-swirl. Flash-Boiling. Ethanol. Nitrous Oxide. Static hot-fire test stand. VOF. Combustion. Instability. Acoustic cavity.

RESUMO

Este relatório apresenta o projeto básico de um injetor e de uma câmara de combustão de motor de foguete para óxido nitroso saturado e etanol líquido, assim como detalhes da construção e operação do motor no qual o injetor será utilizado. De início, realiza-se a seleção de uma mistura oxidante-combustível baseada em uma análise termoquímica que explora diversas opções já existentes e outras combinações ainda pouco estudadas. Como resultado, opta-se por óxido nitroso como oxidante e etanol como combustível. Então uma metodologia simplificada é proposta para o projeto de um injetor do tipo *pressure-swirl* para o etanol. Dinâmica de fluídos computacional é utilizada para verificar a validade da análise supracitada, empregando o método *Volume of Fluid* (VOF). Para o injetor de óxido nitroso, o fenômeno de *flash-boiling* é investigado, verificando-se sua importância para o projeto em andamento. O efeito é tratado analiticamente pelo modelo de Dyer para levar em conta a termodinâmica fora do equilíbrio. Modelos de combustão zero-dimensional e unidimensional são utilizados como ferramentas para o projeto da câmara de combustão do motor. Ainda é apresentado e discutido o fenômeno de instabilidade de combustão em câmaras de combustão de motores de foguete líquido, com o primeiro modo tangencial de oscilação acústico sendo calculado para o motor desenvolvido e um conjunto de cavidades acústicas sendo proposto para amortecer tal modo. Por fim, apresenta-se também um esquema preliminar da bancada de ensaio estático a ser utilizada para testar os injetores e o motor projetado.

Palavras-chave: Motor líquido de foguete. Injetor. Pressure-swirl. Flash-Boiling. Etanol. Óxido Nitroso. Bancada de ensaio estático. VOF. Combustão. Instabilidade. Cavidade acústica.

SUMMARY

LIST OF SYMBOLS

F	thrust	[N]
$\dot{m}_p$	propellant mass flow rate	[kg/s]
P_e	nozzle exit pressure	[Pa]
P_a	ambient pressure	[Pa]
P_c	combustion chamber pressure	[Pa]
A_e	nozzle exit area	[m^2]
A_t	nozzle throat area	[m^2]
V_e	exhaust velocity of gaseous propellant	[m/s]
c	effective exhaust velocity of gaseous propellant	[m/s]
h_i	enthalpy of the gaseous propellant at the nozzle inlet	[J/kg]
h_e	specific enthalpy of the gaseous propellant at the nozzle exit	[J/kg]
k	ratio of specific heats of the gaseous propellant	
$\bar{R}$	universal gas constant	[J/kmol K]
$\mathcal{M}$	molecular weight of gaseous propellant	[kg/kmol]
T_c	combustion chamber temperature	[K]
C_f	thrust coefficient	
η_{C_f}	thrust coefficient efficiency	
c^*	characteristic velocity	[m/s]
η_{c^*}	characteristic velocity efficiency	
g_o	sea level gravitational acceleration	[m/s^2]
I_{sp}	specific impulse	[s]
I_v	volumetric specific impulse	[N s/m^3]
ρ	initial propellant density	[kg/m^3]
OF	oxidiser to fuel mass ratio	
λ	oxidiser to fuel equivalence ratio	
ϕ	fuel to oxidiser equivalence ratio	
$\dot{m}_f$	fuel mass flow rate	[kg/s]
$\dot{m}_{ox}$	oxidiser mass flow rate	[kg/s]
M	local Mach number	
C_{df}	discharge coefficient for fuel injection system	
C_{dox}	discharge coefficient for oxidiser injection system	
A_{if}	injector area for fuel injection system	[m^2]

A_{iox}	injector area for oxidiser injection system	[m^2]
ρ_f	initial fuel density	[kg/m^3]
ρ_{ox}	initial oxidiser density	[kg/m^3]
ΔP_f	pressure drop across fuel injection system	[Pa]
ΔP_{ox}	pressure drop across oxidiser injection system	[Pa]
L_s	spin chamber length	[m]
d_p	inlet port diameter	[m]
d_o	orifice diameter	[m]
β	inlet shot angle	[°]
t	film thickness at exit	[m]
θ	half-cone angle	[°]
σ	fluid surface tension	[N/m]
μ_l	fluid dynamic viscosity	[kg/m/s]
d_{32}	Sauter Mean Diameter	[m]

1 INTRODUCTION

The aerospace sector has been growing in the past years with the introduction of new private-owned companies exploring this market that was previously dominated by governments. With an increasing demand for satellite communication, especially for small satellites, it becomes increasingly more important to own technology to put those satellites in orbit. Rocket engines are one of the main components needed to achieve this goal and, therefore, developing this type of technology will be essential in the near future.

This type of engine has a key component that admits the propellant into the chamber for combustion to occur: the injector. It plays a fundamental role in combustion efficiency, and therefore is crucial on the performance of a liquid-propellant engine. That is why injectors have become so important in rocket engine design, and also in this project.

The present work is part of Project NOELLE (Nitrous-Oxide EthanoL Liquid Engine), whose goal is to design, build and test a small-scale rocket engine prototype with saturated nitrous oxide and liquid ethanol as propellants. The project is subdivided into two main areas: injector and combustion chamber design, presented here, and nozzle and regenerative cooling design, presented in another thesis. Figure 1.1 shows a rendering of Project NOELLE's engine, displaying the nozzle and combustion chamber, built out of copper. Behind the combustion chamber, the fuel and oxidizer injector is seen. Figure 1.2 shows the injector in more detail.

Figure 1.1 – NOELLE rocket engine. The cooled nozzle can be seen in the foreground

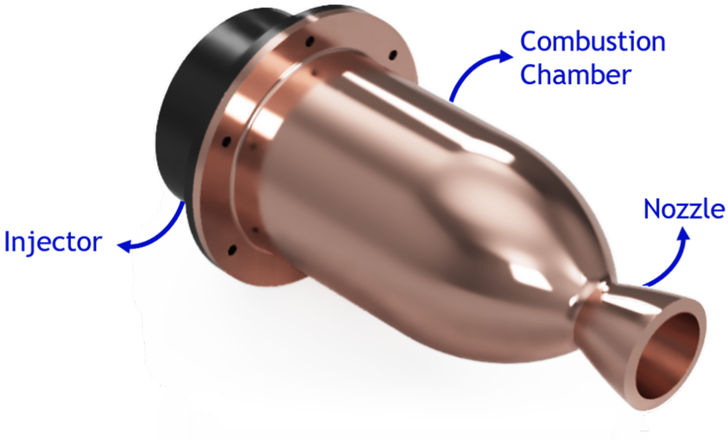

Source: Produced by the authors Ceotto & Tavares

This report starts with an overview of the main objectives and requirements of the injector design. Then, a literature review is carried out, exploring the main topics of interest, such as injector design, flash-boiling, numerical methods related to injectors, multi-phase flows, non-equilibrium thermodynamics and combustion and its associated instabilities.

This is followed by a detailed description of the methodology used in the project. Analytical models are presented for rocket engines, nozzles and injectors. These are then used to compare different fuel-oxidizer mixtures, helping the authors choose a viable candidate. In this case, the preferred choice was nitrous oxide and liquid ethanol. Subsequently, a pressure-swirl injector is chosen for ethanol and the basic equations describing it are explained. On the other hand, a simple orifice injector is chosen for saturated nitrous oxide, and the Dyer et al., 2007 model is employed to determine its geometrical characteristics.

The main results obtained are analyzed. A successful comparison between the analytical and numerical models for the ethanol injector is presented, paving the way to a final design and validation of the rocket engine injector.

Furthermore, a one-dimensional reactor model of vaporization controlled combustion is employed to assess the lifetime of ethanol droplets. Software Cantera is used to simulate a reactor network model, which is used to evaluate the evolution of mass fractions and gas temperature along the combustion chamber, and to compute a suitable chamber length.

Finally, a review on combustion instability is presented, and the first spinning tangential acoustic vibration mode for the herein developed combustion chamber is computed in order to predict at which frequency unstable behaviour might manifest itself. An ensemble of acoustic cavities is designed to suppress the aforementioned mode.

Figure 1.2 – Rocket engine injector for nitrous oxide and liquid ethanol

Source: Produced by the authors Ceotto & Tavares

2 OBJECTIVES

To design the injection system and the combustion chamber of a liquid rocket engine, with the goal of achieving good agreement between a future static fire test and the proposed analytical and numerical models. The geometry of the injector must be such that it allows the propellant to atomize and vaporize, thus supporting combustion. Also, combustion processes and their related instabilities must be taken into account.

Furthermore, the injector shall be well suited for a rocket engine designed with the following prerequisites:

- Engine nominal thrust: 3000 N;
- Engine nominal burn time: 5 s;
- Combustion chamber maximum operating pressure: 15 bar;
- Combustion chamber minimum operating pressure: 1 bar;
- Propellant tank maximum operating pressure: 70 bar;
- Propellant tank minimum operating pressure: 55 bar;

3 LITERATURE REVIEW

3.1 ETHANOL AND NITROUS OXIDE ENGINES

While liquid rocket engines are common in the literature, ethanol - nitrous oxide engines are rather rare and are yet to be implemented as a finished product. (Tokudome et al., 2007) is one of the first published studies to present an operational engine using these propellants. Static-fires were performed achieving 700 N of thrust using like-impinging doublet injectors for both propellants and a gaseous hydrogen - gaseous oxygen torch igniter. While this engine was used as a small scale prototype for further development, (Kakami et al., 2010) designed and tested a much smaller engine with a nominal thrust of 1 N, geared towards small satellites. Besides the different scale, (Kakami et al., 2010) proposed a plasma assisted combustion model, demonstrating its viability.

More recently, (Phillip et al., 2016) developed a modular ethanol - nitrous oxide engine and the necessary infrastructure to conduct further research in the future. Even though the design is similar to (Tokudome et al., 2007) in scale and ignition/injection methods, significantly higher efficiencies were achieved. Important theoretical contributions were also made by (Palacz, 2017) who showed how an ethanol - nitrous oxide engine holds potential for future applications. Among them are launcher vehicles upper stages, storable military units and propulsion for small satellites.

3.2 INJECTION PATTERNS AND ATOMIZATION MODELS

(Sutton and Biblarz, 2016) remains as the standard literature for preliminary analysis and design of rocket propulsion systems. Apart from the mathematical model developed in the present report, the text provides historical and state-of-art information regarding different injection patterns on liquid rocket engines, which is useful when facing the choice of a pattern once the propellant is defined.

(Lefebvre and McDonell, 2017) is regularly cited in the scientific community as a reliable source of information on different injection methods and atomization mechanisms. It includes a comprehensive review of different types of atomizers before delving into the processes of drop breakup and disintegration of liquid sheets. Moreover, it digests empirical correlations found in the literature on the performance of atomizers, with regards to drops size, which can be used for the preliminary design of injectors and for future confrontation with experimental data.

(Xue et al., 2004) discusses the influence of some important geometric parameters on the performance of pressure-swirl atomizers, via the assessment of the discharge coefficient, the dimensionless film thickness and the spray cone half-angle through Computational Fluid Dynamics (CFD) simulations and through an inviscid analysis, from the work of (Giffen and Muraszew, 1953).

(Kang et al., 2018) presents an extensive review on pressure swirl injectors in liquid rocket engines and how it affects the atomization steps of the liquid propellant. The main mechanisms of droplet formations and empirical data retrieved from other studies are displayed in a comprehensive overview. The formation of an air core inside the injector element due to the centrifugal force of the swirling flow is explained, and an empirical relationship is presented for calculating its diameter. The influence of geometrical properties on the discharge coefficient is thoroughly discussed, and a table gathering different empirical equations for its calculation is displayed. These equations are mainly function of the diameter of the tangential inlet port, the diameter and length of the output orifice and the diameter and length of the swirling chamber, which can thus be carefully tuned for the desired discharge coefficient. Moreover, the breakup of the conical liquid film, responsible for the initiation of the atomization process, was covered. Two were said to be parameters of utmost importance: the spray cone angle and the breakup length. The larger the first one, the smaller the latter. Different spray patterns were introduced, and the spray cone angle is given an equation for computing it, which is also a function of geometrical properties of the injector.

3.3 NUMERICAL SIMULATION OF PRESSURE-SWIRL INJECTORS

(Maly, Jedelsky, et al., 2018) and (Maly, Slama, et al., 2019) discuss the numerical simulation of a pressure-swirl atomizer by taking advantage of the axisymmetry of the problem. The Volume of Fluid (VOF) method from ANSYS Fluent commercial software is employed to good agreement with experimental data, using a laminar model. (Sun et al., 2018), on the other hand, reveals itself as a good review of the analytical model and on numerical simulation of sprays using the Discrete Phase Model (DPM).

3.4 NITROUS OXIDE INJECTION SYSTEM

Flash-boiling will later in the text present itself as an additional challenge to the design of the nitrous oxide injector.

(Sher, Bar-Kohany, and Rashkovan, 2008) presents a detailed review of the different mechanisms which may occur during flash-boiling. These include intense nucleation, fast bubbles' growth and liquid atomization. The explanation is followed by an example of an injector specifically designed to take advantage of flash-boiling. The main contribution of this publication to the current project is the general understatement of what flash-boiling is and how it can be modeled analytically or semi-empirically.

(Lyras et al., 2018), on the other hand, focuses on modeling flash-boiling phenomena in injectors by means of numerical methods. It describes the implementation of a new OpenFOAM solver named FlashFOAM specifically tailored for this application, accounting for the inter-phase heat transfer using the Homogeneous Relaxation Model (HRM). Furthermore, the numerical results are validated against NASA flash-boiling injectors of cryogenic liquid oxygen.

Much simpler than the analytical and numerical methods cited so far, (Dyer et al., 2007) proposed a method to model simple orifice nitrous oxide injectors. After arguing that nitrous oxide can have an intermediate behaviour between a single-phase incompressible fluid and a multi-phase fluid undergoing isentropic expansion, they proposed a weighted average of the mass flow rate predicted by both models, in which the contribution of each is considered by the characteristic bubble growth time and the residence time of the liquid inside the injector. Furthermore, (Dyer et al., 2007) also presented important contributions in the modelling of the thermodynamic properties of nitrous oxide by describing the parameters of a Span-Wagner Helmholtz-Explicit Equation of State for the substance.

Unfortunately, the analytical model presented by (Dyer et al., 2007) was shown to have a mistake, which was later corrected by (Solomon, 2011) and further acknowledged by (Waxman et al., 2013) and (Whitmore and Chandler, 2010).

(Waxman et al., 2013) used nitrous oxide in an experimental setup in order to determine the effects of injector geometry on the atomization of fluid particles, presenting results with good agreement to (Dyer et al., 2007)'s model corrected by (Solomon, 2011). (Gamper and Hink, 2013) also provides useful insight on the effectiveness of different injector patterns by comparing those through cold test experiments on a test bench. Nitrous oxide was used as the working fluid, and the discharge coefficients were computed through the obtained experimental data.

3.5 COMBUSTION MODELING

(Turns, 1996) constitutes the main source for the ordinary differential equations which govern a reactor. Meanwhile, (Marinov, 1999), (Saxena and Williams, 2007) and (Cancino et al., 2010) discuss reaction mechanisms used for ethanol-air combustion, while (MONAT, HANSON, and KRUGER, 1977) provides the mechanisms involved in nitrous oxide decomposition.

3.6 COMBUSTION INSTABILITY

Although it has been extensively studied (and witnessed through failures), the phenomenon of combustion instability still inspires caution, especially because the reasons behind its onset are not perfectly understood. Nevertheless, it is of paramount importance on the design of liquid rocket engines, since neglecting it might lead to unwanted explosions. Although it cannot yet be accurately predicted, it can be understood: (Zucrow and Hoffman, 1977) presents the underlying theory behind combustion instability, deriving the acoustical modes of oscillation (inside a cylindrical cavity) that may become unstable. On the other hand, (Bennewitz and Frederick, 2013) discuss traditional and novel methods for suppressing these instabilities, specifically passive techniques, like baffles. (Kim, 2010) reveals itself a useful source on the design of small acoustic cavities, which are another type of passive control devices.

4 ROCKET ENGINE DESIGN

4.1 PRELIMINARY MATHEMATICAL MODEL

There are three major constraints that are considered in the early stages of propulsion system design: thrust, chamber pressure and ambient pressure. Once these are set and the propellant is chosen, it is possible to compute the main parameters of a rocket engine.

4.1.1 PERFORMANCE

From Newton's Third Law, the thrust generated by a rocket motor can be defined as:

$$F = \dot{m}_p V_e + (P_e - P_a) A_e \tag{4.1}$$

Where the first term constitutes a dynamic contribution and the second one constitutes a static contribution to the thrust. Rearranging the equation, one finds:

$$F = \dot{m}_p \left(V_e + \frac{(P_c - P_a) A_e}{\dot{m}_p} \right) = \dot{m}_p c \tag{4.2}$$

Where c is defined as the effective exhaust velocity of the gaseous propellant. When an optimal expansion is considered through the nozzle (which will be the case in the present report from now on), P_e matches P_a and therefore c equals V_e.

For an adiabatic, no shaft-work steady inviscid flow inside the nozzle, the exhaust velocity of the gaseous propellant can be obtained by applying the first law of thermodynamics to a control volume comprising the inlet section and the outlet section of the nozzle, which yields:

$$V_e = \sqrt{2(h_i - h_e) + V_i^2} \tag{4.3}$$

Where the subscripts i and e refer to the nozzle inlet and outlet sections, respectively. In the preliminary design, further assumptions are made:

1. The products from combustion are homogeneous, gaseous and obey the perfect gas law;
2. Combustion chamber is adiabatic;
3. Stagnation condition at the inlet section of the nozzle;
4. Isentropic flow across the nozzle (no friction losses or shock waves);
5. The composition of the exhaust gas does not change along the nozzle (frozen flow).

Thus equation 4.3 can be rewritten, using isentropic flow relations, as:

$$V_e = \sqrt{\frac{2k}{k-1}\frac{\bar{R}T_c}{\mathcal{M}}\left(1-\left(\frac{P_e}{P_c}\right)^{\frac{k-1}{k}}\right)} \tag{4.4}$$

It is noticeable that, in order to increase the exhaust velocity of the gas, the ratio between exit pressure P_e and chamber pressure P_c can be increased. Moreover, the chamber temperature T_c (here considered to be the adiabatic flame temperature) can be increased and the molar mass of the gaseous products $\mathcal{M}$ can be decreased. The latter two are dependent on the propellant selection, whereas the former is an input of the design process.

The exhaust velocity equation can be further rewritten in order to distinguish between the propellant thermochemical contribution and the nozzle mechanical contribution:

$$V_e = C_f c^* \tag{4.5}$$

Where C_f is called thrust coefficient, which represents an increment on the gas exhaust velocity due to its expansion on a supersonic nozzle. It is dimensionless and is given by:

$$C_f = \sqrt{\frac{2k^2}{k-1}\left(\frac{2}{k+1}\right)^{\frac{k+1}{k-1}}\left(1-\left(\frac{P_e}{P_c}\right)^{\frac{k-1}{k}}\right)} + \frac{P_e - P_a}{P_c}\frac{A_e}{A_t} \tag{4.6}$$

When considering an optimal expansion, the exit pressure P_e matches the ambient pressure P_a, and the second term vanishes. In order to take into account irreversibility processes during expansion and the fact that not all exhaust gases have an axially directed velocity when leaving the nozzle, a thrust coefficient efficiency, η_{C_f}, is usually considered.

The characteristic velocity c^* is only dependent on the propellant characteristics and the combustion chamber design. Although it has m/s units, it is not a velocity *per se*. It is a measure of combustion performance, given by:

$$c^* = \frac{\sqrt{\frac{k\bar{R}T_c}{\mathcal{M}}}}{k\sqrt{(\frac{2}{k+1})^{\frac{k+1}{k-1}}}} \tag{4.7}$$

In order to take into account combustion instability phenomena, a characteristic velocity efficiency, η_{c^*}, is usually considered.

Since the thrust is a design input, once the exhaust velocity is computed one can determine the propellant mass flow rate $\dot{m}_p$ by solving equation 4.1.

Another important parameter is the specific impulse, which is defined as the ratio between thrust and the sea level weight rate of propellant consumption at a given instant of time, as follows:

$$I_{sp} = \frac{T}{\dot{m}_p g_o} \tag{4.8}$$

Therefore, I_{sp} can be seen as a merit of propellant efficiency. For non-constant thrust, I_{sp} is defined as:

$$I_{sp} = \frac{\int_{t_o}^{t_b} F dt}{\int_{t_o}^{t_b} \dot{m}_p g_o dt} \tag{4.9}$$

Where t_b is the burn time.

Furthermore, it is possible to define the volumetric specific impulse, which can be seen as a measure of how much energy can be stored inside a rocket engine of a given size. The higher the volumetric specific impulse, the higher the energy that can be stored. It is defined as:

$$I_v = \rho I_{sp} \tag{4.10}$$

Once $\dot{m_p}$ is computed, it is possible to determine the mass flow rate of both the fuel and the oxidiser given the oxidiser to fuel mass ratio, written as:

$$OF = \frac{\dot{m_{ox}}}{\dot{m_f}} \tag{4.11}$$

Hence:

$$\dot{m_{ox}} = \frac{OF}{1+OF}\dot{m_p} \tag{4.12}$$

$$\dot{m_f} = \frac{1}{1+OF}\dot{m_p} \tag{4.13}$$

The I_{sp} is highly sensitive with respect to OF. Therefore, the latter is usually chosen such as the former is maximized.

4.1.2 NOZZLE

Simply stated, the nozzle is a device that converts thermal energy into mechanical energy, by expanding the gaseous propellant at high temperature and pressure into the surroundings.

From equation 4.4, but considering a control volume between the inlet section of the nozzle (stagnation condition) and an arbitrary section along the nozzle:

$$T_i = T_c = T + \frac{v^2}{C_p} \tag{4.14}$$

Substituting by the Mach number (ratio between the flow velocity and the local speed of sound):

$$\frac{T_c}{T} = 1 + \frac{k-1}{2}M^2 \tag{4.15}$$

Considering the continuity equation, an isentropic flow across the nozzle and that the Mach number is equal to unit at the throat, it can be shown that:

$$\frac{A}{A_t} = \frac{1}{M}\left(\frac{1+\frac{k-1}{2}M^2}{1+\frac{k-1}{2}}\right)^{\frac{k+1}{2(k-1)}} \tag{4.16}$$

Which reveals that, in order for the gaseous propellant to be accelerated to supersonic velocities, the nozzle must have a convergent-divergent section profile.

Making further use of isentropic flow relations between temperature, pressure and density, it is possible to find the following relationship:

$$\frac{A_t}{A_e} = \left(\frac{k+1}{2}\right)^{\frac{1}{k-1}} \left(\frac{P_e}{P_c}\right)^{\frac{1}{k}} \sqrt{\left(\frac{k+1}{k-1}\right)\left(1-\left(\frac{P_e}{P_c}\right)^{\frac{k-1}{k}}\right)} \tag{4.17}$$

Substituting equation 4.6 into equation 4.1 yields:

$$F = C_f A_t P_c \tag{4.18}$$

For optimal expansion condition C_f does not depend on A_t, and therefore the latter is the only unknown in the above equation.

Since A_t is known, A_e can be calculated by solving equation 4.17.

4.1.3 INJECTION SYSTEM

The injection system is responsible for properly admitting both the oxidiser and the fuel into the combustion chamber, thus allowing those to atomize and vaporize. By increasing the active surface area of the fluid particles, these steps play a fundamental role in combustion efficiency and therefore are defining on the performance of a liquid-propellant engine.

From Bernoulli equation, for an incompressible flow across a restriction orifice, the mass flow rate is shown to be:

$$\dot{m} = C_d A_i \sqrt{2\rho \Delta P} \tag{4.19}$$

Where C_d is the discharge coefficient, a correction factor that takes into account non-isentropic phenomena due to viscosity. It is a function of the orifice geometry. A_i is the area of the orifice (or the sum of the areas from all the orifices on a plate).

On a liquid-propellant engine, the injection plate bears distinct groupings of injection orifices, for fuel and oxidiser. Therefore:

$$\dot{m}_f = C_{df} A_{if} \sqrt{2\rho_f \Delta P_f} \tag{4.20}$$

$$\dot{m_{ox}} = C_{dox} A_{io} \sqrt{2 \rho_{ox} \Delta P_{ox}} \tag{4.21}$$

The arrangement of these orifices with respect to each other (injection pattern) is crucial to achieving a correctly proportioned mixture of oxidiser and fuel at given point in the combustion chamber.

4.2 PROPELLANT SELECTION

In order to select an appropriate oxidizer and fuel pair, several conditions were considered. First, the existence of suppliers greatly limits the possible fluids to be considered.

In fact, supply was the first criteria used for screening. Based on local availability, the oxidizers and fuels considered for the following analysis are presented in Table 4.1.

Table 4.1 – List of oxidizers and fuels to be analyzed based on aviability screening.

Considered Oxidizers and Fuels List	
Oxidizers	Fuels
Liquid Oxygen - LOX	Liquid Methane - LCH4
Gaseous Oxygen - GOX	Gaseous Methane - GCH4
Nitrous Oxide - NOX	Ethanol - C2H5OH
	JetA - C12H23

Considering the 3 oxidizers and 4 fuels selected, 12 possible oxidizer-fuels pairs can be formed. Each pair was analyzed using the mathematical model described in chapter 4.

As a result, two main important parameters were selected for comparison, the specific impulse I_{sp} and the volumetric specific impulse I_v.

For each oxidizer-fuel pair, a range of optimal operation was simulated and plotted in Figure 4.1. The developed code used for this analysis, which is based on NASA Chemical Equilibrium with Applications (NASA CEA) program output, is available at GitHub (Ceotto, Dias, and Tavares, 2020).

In terms of specific impulse, slight variation between propellant combinations can be seen. In general, all combinations presented a specific impulse between 200 s and 250 s. The propellants can be naturally divided into two groups: propellant combinations of low density and of high density. Any combination in which at least one of the fluids is in a gaseous state, will have an overall low density. Higher density combinations are desired since they require smaller propellant tanks, crucial in a rocket. Thus, Figure 4.2, displays only propellants in which both fuel and oxidizers can be stored as a liquid or at least in a liquid-saturated state. These are the combinations considered from here.

Figure 4.1 – Specific impulse of all considered oxidizer-fuel combinations.

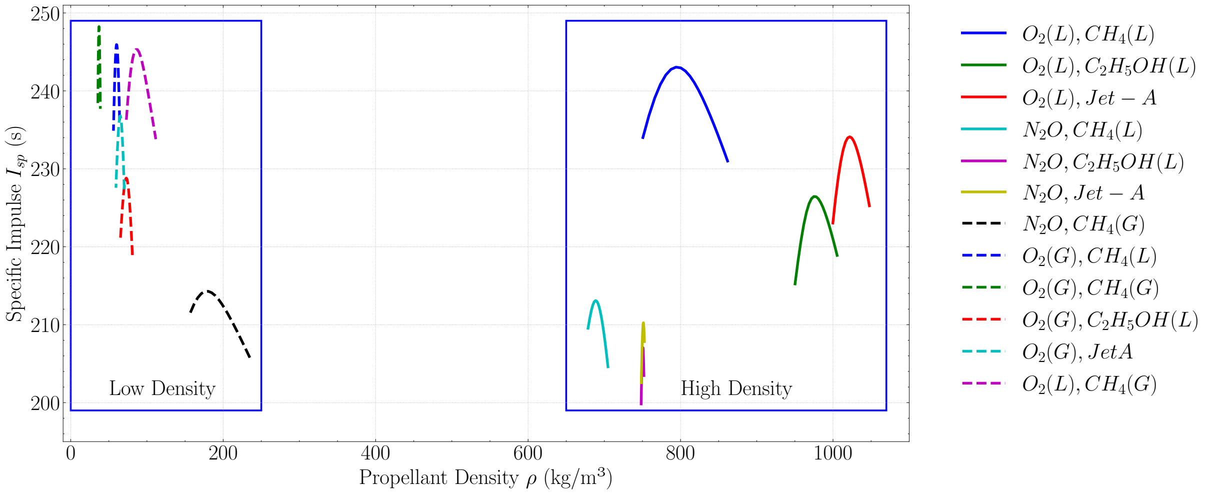

Source: Produced by the authors Ceotto & Tavares

Figure 4.2 – Specific impulse of oxidizer-fuel combinations in which both are liquid.

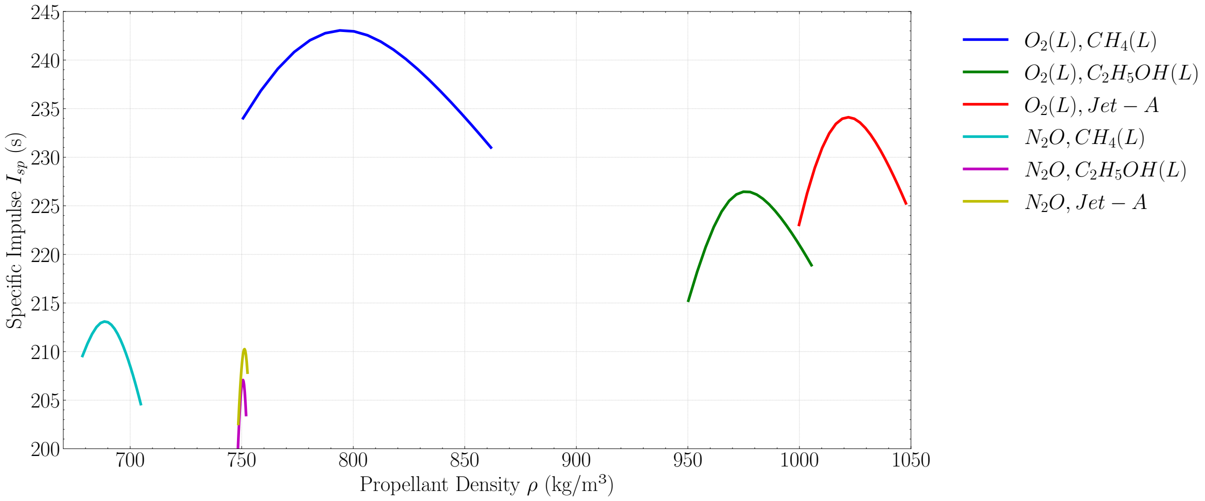

Source: Produced by the authors Ceotto & Tavares

Although some combinations provide a substantial advantage in terms of specific impulse, they fell out of favor due to the comparatively higher difficulty in purchasing one or both of the components. This is the case of propellants including JetA, Liquid Oxygen and Liquid Methane, that were only found to be sold in extremely large amounts, usually to industries.

Moreover, it was later decided not to use any gaseous substance, since these lead to comparatively low volumetric specific impulses, which in turn make the use of the respective rocket engine prohibitive due to overall weight concerns.

Therefore, it was decided to proceed with a Nitrous Oxide and Ethanol powered rocket motor. Among their advantages, it is worth noting the self-pressurization properties of the Nitrous Oxide (which dismisses the need for additional pressurization devices) and the low freezing point of Ethanol, which makes it suitable for regenerative cooling the nozzle.

4.3 ENGINE PARAMETERS: N2O, C2H5OH(L)

Considering the use of nitrous oxide (N2O) as oxidiser and liquid ethanol (C2H5OH(L)), the rocket engine was simulated employing the model described above. A fuel to oxidiser equivalence ratio ϕ of 1.5 was considered in order to yield a low adiabatic chamber temperature and allow the successful regenerative cooling of the nozzle. The resulting quantities obtained can be analyzed in Table 4.2.

It is worth noting that the values for nominal chamber pressure and pressure on the fuel inlet are such as to enable proper regenerative cooling of the nozzle. The pressure of ethanol inside the cooling channels (that is, before entering the injector) should be above its critical pressure, in order to prevent nucleate boiling regime (Sutton and Biblarz, 2016). Moreover, it must be pointed out that the fuel is actually a mixture of ethanol and water, with 92% by mass of ethanol and 8% of water, in order to enhance the convection heat transfer coefficient. Finally, some of the fuel will be injected to sustain film cooling: this portion of the fuel will not be considered when designing the ethanol injector.

Table 4.2

– Specified and calculated rocket engine parameters using N2O as oxidizer and C2H5OH(L) as fuel.

Parameter	Value	Unit
Thrust	3000.00	[N]
Burn time	5.00	[s]
Chamber pressure	15.0	[bar]
Adiabatic chamber temperature	2938.2	[K]
Molecular Weight of exhaust products	24.2	[kg/kmol]
Fuel to oxidiser equivalence ratio	1.5	-
Ratio of specific heats of exhaust products	1.17	-
Oxidiser/fuel mass ratio	3.52	-
Pressure on oxidiser tank	56.52	[bar]
Temperature on oxidiser tank	298.15	[K]
Pressure on fuel inlet	∼ 63.00	[bar]
Temperature on fuel inlet	370.0	[K]
Characteristic velocity	1563.16	[m/s]
Thrust coefficient	1.36	-
Specific impulse	216.66	[s]
Total mass flow rate	1.411	[kg/s]
Oxidiser mass flow rate	1.099	[kg/s]
Fuel mass flow rate (injector)	0.209	[kg/s]
Fuel mass flow rate (film cooling)	0.104	[kg/s]
Total oxidiser mass	5.494	[kg]
Total fuel mass	1.563	[kg]
Nozzle throat diameter	43.3	[mm]
Nozzle exit diameter	75.8	[mm]

5 ETHANOL INJECTOR

Since the behaviour of the chosen liquid propellants greatly differ at the Standard Ambient Temperature (nitrous oxide is on the saturation region, while ethanol is compressed liquid), independent analyses were carried out to determine the injection method for each propellant, which led to the final injection pattern.

For the single-phase flow of ethanol, the pressure-swirl atomizer was deemed more suitable than the others, mainly due to its wide range of applications, to the extensive available literature and to its characteristic low discharge coefficient (Lefebvre and McDonell, 2017), which allows for a great pressure drop (essential to ensure proper liquid breakup). In this type of injector, the liquid is imparted with a swirling motion, and under the resulting centrifugal force a conical sheet is formed as the fluid leaves the atomizer.

5.1 PRESSURE-SWIRL ANALYTICAL MODEL

A typical pressure-swirl simplex atomizer is shown in Figure 5.1.

On pressure-swirl atomizers the high-pressure liquid enters a spin chamber of length L_s through tangential inlet ports of diameter d_p. As a result the fluid not only has an axial velocity component, but also a tangential velocity component, which leads to the swirling motion and to the emergence of an air-core. It then proceeds to the orifice of diameter d_o, forming a thin liquid sheet of thickness t that disintegrates as it leaves the atomizer, in a conical shape: it becomes unstable and breaks up into droplets.

Unfortunately, the dynamics of the fluid inside the simplex atomizer are quite complex, with unsteady and turbulent behaviour to be expected (Xue et al., 2004). Nevertheless, the inviscid analysis from the work of (Giffen and Muraszew, 1953), later modified by (Xue et al., 2004) to account for additional parameters, yields useful and somewhat accurate relationships between performance and geometric parameters, and thus was the cornerstone for the preliminary design of the ethanol injector.

The conservation of angular momentum yields the following relationship between tangential velocity w and radius r:

$$\omega r = \omega_i r_i = \text{constant} \tag{5.1}$$

Figure 5.1 – Schematic of a simplex pressure-swirl atomizer.

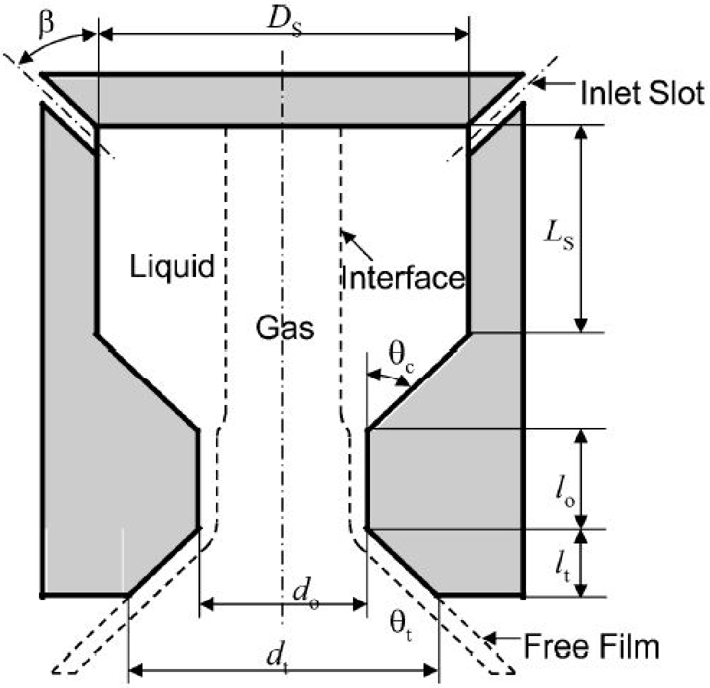

Source: (Xue et al., 2004)

Figure 5.2 – Top view of a simplex pressure-swirl atomizer.

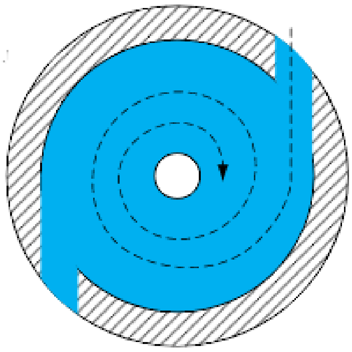

Source: (Kang et al., 2018)

Where i denotes inlet conditions. The tangential velocity at the inlet can be calculated by:

$$\omega_i = Q \sin\beta / A_p \tag{5.2}$$

Where Q is the volume flow rate through a single inlet port, A_p is the area of the inlet port and β is the angle of the inlet port with the atomizer axis of symmetry. β usually assumes a value of 90°.

Considering the flow incompressible, irrotational and stationary, Bernoulli's equation can be applied to calculate the total pressure, p_t, of the fluid going through the inlet port:

$$p_t = p + \frac{\rho u^2}{2} + \frac{\rho w^2}{2} \tag{5.3}$$

Where p is the gauge static pressure at the inlet port, ρ is the fluid's density and u is the axial velocity component. This total pressure must be constant, considering the hypothesis made above. Therefore, the fluid right at the exit of the atomizer, adjacent to the inner air core formed, shall have a total pressure given by:

$$p_t = \frac{\rho u_e^2}{2} + \frac{\rho w_e^2}{2} \tag{5.4}$$

Where the e subscript represents exit condition. Notice how the gauge static pressure is assumed to be zero. This means that p effectively represents the difference in the static pressure of the inlet and outlet of the atomizer.

Furthermore, u_e and w_e can be expressed by:

$$u_e = \frac{Q}{A_o - A_e} \tag{5.5}$$

$$w_e = \frac{Q r_i \sin\beta}{A_p r_e} \tag{5.6}$$

Where A_o is the exit orifice area $(\pi d_o^2/4)$, A_e is the area of the air core at the exit (πr_e^2). Substituting results in:

$$p_t = \frac{\rho}{2}\left(\left(\frac{Q}{A_o - A_e}\right)^2 + \left(\frac{Q r_i \sin\beta}{A_p r_e}\right)^2\right) \tag{5.7}$$

Using the definition of the discharge coefficient C_d:

$$Q = C_d A_e \sqrt{\frac{2p_t}{\rho}} \tag{5.8}$$

$$\frac{1}{C_d^2} = \frac{1}{(1-X)^2} + \frac{1}{K_1^2 X}\frac{r_i}{r_s}\sin^2\beta \tag{5.9}$$

Where r_s is the radius of the swirl chamber, and K_1 and X are given by:

$$X = \frac{A_e}{A_o} \tag{5.10}$$

$$K_1 = \frac{A_p}{\pi r_o r_s} \tag{5.11}$$

To solve the problem, a strong assumption shall be made. The size of the air core shall be such that the maximum flow rate possible is achieved. That means that C_d will be the maximum possible. This implies that:

$$C_d = \sqrt{\frac{(1-X)^3}{(1+X)}} \tag{5.12}$$

It is important to notice that X is directly related to the thickness of the film formed due to the constant mass flow rate. The relation is expressed by:

$$\frac{t}{r_o} = 1 - \sqrt{X} \tag{5.13}$$

Comparing u_e and w_e leads directly to the spray cone half angle, θ, given by:

$$\theta = \arctan w_e/u_e \tag{5.14}$$

It is important to notice that the three equations 5.12, 5.13, 5.14 are of extreme importance in the design of the pressure-swirl injector. They will be used to define the preliminary geometrical parameters of the injector considering the pressure difference between the combustion chamber and propellant tank as well as the mass flow rate as inputs.

Notice however an empirical correction to equation 5.12. (Giffen and Muraszew, 1953) proposed the correction coefficient of 1.17 to fit experimental data, resulting in the equation 5.15:

$$C_d = 1.17\sqrt{\frac{(1-X)^3}{(1+X)}} \tag{5.15}$$

This correction coefficient was proposed assuming $\frac{r_i}{r_s} = 1$ and $\beta = 90°$ in the model, and thus these will be considered for the injector design.

Finally, another important parameter for assessing the performance of the atomizer is the Sauter Mean Diameter (SMD), which is defined as the "diameter of a droplet whose surface-to-volume ratio is equal to that of the entire spray" (Lefebvre and McDonell, 2017). The smaller the SMD, the bigger the surface area of the droplet with respect to its own volume, and therefore the better the atomization process. (Lefebvre and McDonell, 2017) proposes an empirical formula for computing the SMD, considering the disintegration of the liquid sheet due to hydrodynamic and aerodynamic forces, followed by the break down of surface protuberances into ligaments and droplets:

$$SMD = 4.52\left(\frac{\sigma {\mu_l}^2}{\rho_A \Delta {P_l}^2}\right)^{0.25} (tcos\theta)^{0.25} + 0.39\left(\frac{\sigma \rho_l}{\rho_A \Delta P_l}\right)^{0.25} (tcos\theta)^{0.75} \tag{5.16}$$

Where σ is the surface tension of the fluid, μ_l its dynamic viscosity, ρ_l its density, ρ_A the density of the ambient medium and ΔP_l the pressure drop.

5.2 NUMERICAL MODEL

In order to more accurately predict the performance of the ethanol injector, two different numerical simulations were intended to be carried out on ANSYS Fluent software: one to evaluate the flow inside the atomizer and the primary liquid breakup, using the Volume of Fluid (VOF) method, and the other to evaluate the secondary breakup process and the resulting average particle size, or Sauter Mean Diameter, using the Discrete Phase Model (DPM). Due to the lack of available computational infrastructure, only the former was executed. Future work will carry out the latter using a VOF-to-DPM model transition mechanism available in Fluent, in which droplets originated in the VOF simulation are converted to Lagrangian particle parcels. This will allow the assessment of the SMD, and will also be useful for further combustion simulations. Nevertheless, both models employed in each of these simulations are briefly explained in the following subsections.

5.2.1 VOLUME OF FLUID

The Volume of Fluid (VOF) method was chosen in order to accurately track the injector's air-core, to validate the analytical model proposed by (Giffen and Muraszew, 1953) and to generate a primary breakup of the liquid sheet that would allow the future use of the DPM model.

The VOF method is recommended for tracking the interface between two immiscible fluids, which makes it suitable for computing the internal flow on the pressure-swirl atomizer and for capturing the internal air-core. It solves a continuity equation for each of the phases and a single momentum equation, and keeps track of the volume fraction of each of the fluids in each computational cell. It assumes incompressible flow and uniform dynamic viscosity.

The VOF method relies on solving the differential form of the continuity and momentum equation in conservation form for the fluid (the latter being commonly known as the Navier-Stokes equations). The continuity equation is written as:

$$\frac{\partial \rho}{\partial t} + \nabla . \left(\rho \vec{V}\right) = 0 \tag{5.17}$$

Whereas the Navier-Stokes equations are defined as follows:

$$\frac{\partial \left(\rho \vec{V}\right)}{\partial t} + \nabla . \left(\rho \vec{V} \vec{V}\right) = -\nabla p + \nabla . \left[\mu \left(\nabla \vec{V} + \nabla \vec{V}^T\right)\right] + \rho \vec{g} \tag{5.18}$$

Where the left-hand side of the equation comprises the acceleration terms, while the right-hand side describes both the internal forces (due to differential pressure and viscosity) and the external forces (such as the gravitational force) acting on an infinitesimal fluid element.

The VOF method solves the continuity equation for each cell of the discretized domain, taking into account multiple phases inside this cell, as aforementioned. Thus the equation to be solved is sightly different from the previously shown, and it must be computed for each phase. It is written as (Ansys, 2020):

$$\frac{1}{\rho_q}\left[\frac{\partial}{\partial t}\left(\alpha_q\rho_q\right)+\nabla.\left(\alpha_q\rho_q\vec{v_q}\right)=S_{\alpha_q}+\sum_{p=1}^{n}\left(\dot{m}_{pq}-\dot{m}_{qp}\right)\right] \tag{5.19}$$

Where α_q corresponds to the volume fraction of the phase q, ρ_q to the density of the pahse q, $\overrightarrow{v_q}$ to the velocity vector of the phase q, $\dot{m}_{pq}$ to the mass transfer from phase p to phase q, $\dot{m}_{qp}$ to the mass transfer from the phase q to the phase p and S_{α_q} to a source term, which by default is zero. It can be solved using the implicit or the explicit formulation. When the implicit formulation is used, the continuity equation is discretized in the following fashion:

$$\frac{{\alpha_q}^{n+1}{\rho_q}^{n+1}-{\alpha_q}^{n}{\rho_q}^{n}}{\Delta t}V+\sum_{f}({\rho_q}^{n+1}{U_f}^{n+1}{\alpha_{q,f}}^{n+1})=[S_{\alpha_q}+\sum_{p=1}^{n}\left(\dot{m}_{pq}-\dot{m}_{qp}\right)]V \tag{5.20}$$

Where $n+1$ corresponds to the index for the current time step, n to the index for the previous time step, ${\alpha_{q,f}}^{n+1}$ to the face value of the q^{th} volume fraction at time step $n+1$, ${U_f}^{n+1}$ to the volume flux through the face at time step $n+1$ and V to the cell volume.

The primary-phase volume fraction is computed according to the following constraint:

$$\sum_{q=1}^{n}\alpha_q=1 \tag{5.21}$$

The momentum equation to be solved is the following:

$$\frac{\partial}{\partial t}\left(\rho\vec{v}\right)+\nabla.\left(\rho\vec{v}\,\vec{v}\right)=-\nabla p+\nabla.\left[\mu\left(\nabla\vec{v}+\nabla\vec{v}^{T}\right)\right]+\rho\vec{g}+\vec{F} \tag{5.22}$$

With the density ρ and the dynamic viscosity μ being dependent on the volume fraction of all the phases, being calculated by volumetric averaging over the phases.

The VOF method can also take into account evaporation (through energy equation), turbulence and surface tension models, if activated. However, this was not used.

For interface tracking, ANSYS Fluent applies a special interpolation scheme in the mesh cells near the interface between the two immiscible fluids. One of the available schemes, the Geometric Reconstruction, was used. It assumes the interface is represented by a linear slope within each cell, whose position relative to the center of the cell must first be determined by the computed volume fraction and its derivatives. Then it calculates fluid advection through each face, taking into account the linear interface representation. Finally, volume fraction is computed through the balance of fluxes previously calculated.

Figure 5.3
– Comparison between actual interface and assumed interface on the Geometric Reconstruction method.

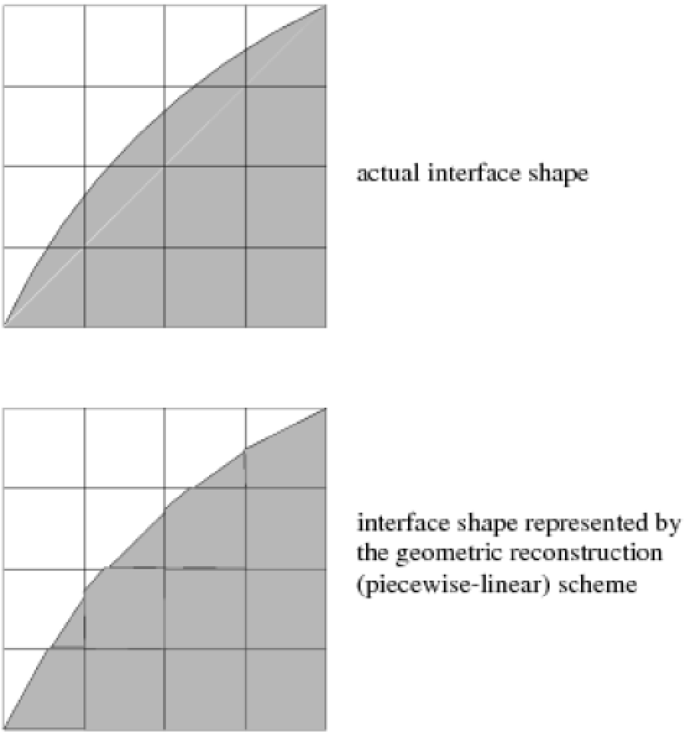

Source: (Ansys, 2020)

5.2.2 DISCRETE PHASE MODEL

The Discrete Phase Model (DPM) solves the Navier-Stokes equation for the fluid phase, as it treats it as a continuum, while tracking each particle of the discrete phase that is travelling through the medium in a Lagrangian approach. The DPM may account for discrete phase inertia, heating/cooling, aerodynamic drag, vaporization and turbulent effects, among others. This set of effects influence the calculated trajectory of the particles using the Lagrangian formulation.

The planned DPM simulation would have neglected the effects of radiation heat transfer to the particles, of collision between particles and of gravity. Furthermore, the Species Transport model would have been enabled in order to allow the mixing of the vapour phase of ethanol with the continuum fluid; this is specially important in combustion simulations.

In order to assess the atomization process, the Sauter Mean Diameter (SMD) inside each cell is computed by the software in the following fashion:

$$d_{32} = \frac{\sum N_i L_i^3}{\sum N_i L_i^2} \tag{5.23}$$

Where N_i refers to the i-th child particle and L_i refers to the length of the i-th child particle inside the cell. The SMD can be defined as the diameter of the particle whose ratio of volume to surface area is equal to that of all the other particles of the spray.

5.3 ANALYSES AND RESULTS

Taking into account the requirement for ethanol mass flow rate (presented in table 4.2), a pressure-swirl atomizer was designed following the analysis discussed in section 5.1. The goal was to impart the liquid with enough angular momentum to yield a SMD of 40 μm or greater on the combustion chamber, to avoid the evaporation of ethanol droplets to occur too close to the injection plate, possibly leading to the melting of the latter. After some iterations, one design was deemed suitable, and then the outputs of the analytical model were confronted with the outputs of the numerical simulations using ANSYS Fluent.

The outputs from the analytical model were computed using a Python code, which can be found on GitHub (Ceotto, Dias, and Tavares, 2020). CoolProp (Bell et al., 2014) was used for retrieving ethanol properties.

5.3.1 INPUTS OF THE ANALYTICAL MODEL

The inputs for the ethanol injector design process were:

Table 5.1 – Inputs for the ethanol pressure-swirl atomizer analytical model

Parameter	Value	Unit
Fuel temperature	370	[K]
Ambient gas density	1.486	[kg/m^3]
Combustion chamber pressure	15.0	[bar]
Fuel inlet pressure	$\sim$ 63.0	[bar]
Fuel density	745.0	[kg/m^3]
Fuel mass flow rate	0.209	[kg/s]
Inlet shot angle	90	[°]
Orifice diameter	2.5	[mm]
Diameter of each inlet slot	1.75	[mm]
Ratio of spin chamber diameter over orifice diameter	2	-
Number of inlet slots	4	-

5.3.2 OUTPUTS OF THE ANALYTICAL MODEL

The relevant outputs from the analytical model were the following:

Table 5.2 – Outputs from the ethanol pressure-swirl atomizer analytical model

Parameter	Value	Unit
Discharge coefficient	0.5067	
Fuel inlet pressure	62.4	[bar]
Film thickness	0.495	[mm]
Spray cone half-angle	40.1	[°]
Expected Sauter Mean Diameter	40.0	[μm]

5.3.3 SPRAY CONE HALF-ANGLE AND FILM THICKNESS USING VOF

In order to simulate the internal flow inside the pressure-swirl atomizer, the axisymmetry of the problem was taken into account and therefore a 2D mesh was made. The inlet was constructed as an edge of length equal to the inlet ports diameter. The 2D-axisymmetric model is depicted by Figure 5.4

The inlet boundary condition was set to velocity, with a swirling (tangential) velocity of 18.955 m/s, corresponding to the mean fluid velocity on the inlet port times the ratio between the distance from the inlet port axis to the swirl chamber axis and the diameter

Figure 5.4 – Refined mesh at simulation end with boundary conditions

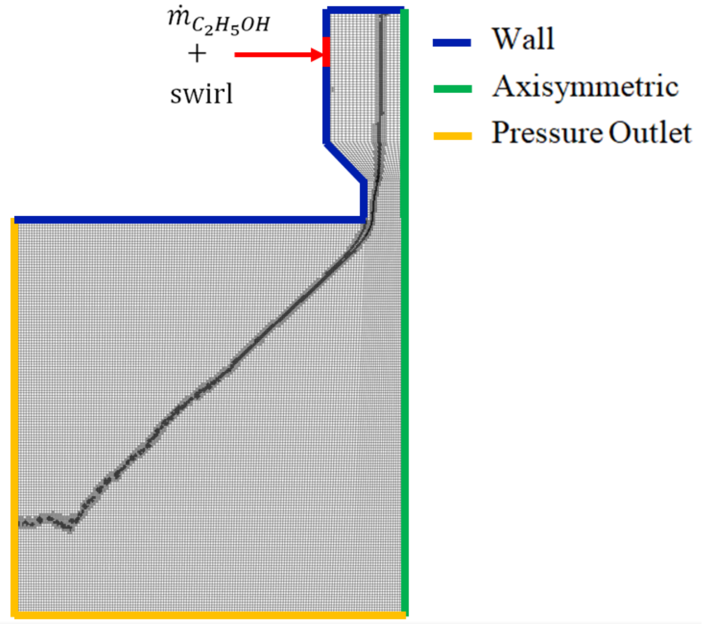

Source: Produced by the authors Ceotto & Tavares

of the swirl chamber (to conserve angular momentum), while the radial velocity was set as 10.206 m/s to conserve the mass flow rate. Back-flow pressure was set to the outlet boundary condition, and a no-slip condition was imposed to the walls. The flow was treated as laminar: in (Maly, Slama, et al., 2019), the laminar model provided results with good agreement to experimental data, and thus was deemed suitable.

The transient VOF model was computed using a PISO scheme with first order implicit time integration. A variable time step size of between 1e-06 s and 1e-08 s was used, maintaining the maximum Courant number value equal to 1. The volume fraction equation was solved using a explicit time integration method which employed sub-timesteps with the goal of keeping the maximum Courant number value below 0.25. The interface between the air phase and the ethanol phase was tracked using geometric reconstruction and mesh adaptation was employed to refine the domain in these regions. Figure 5.4 shows the refined mesh at the last step of the of the time integration.

The model was simulated until the total inlet pressure reached a stable value, usually after 2.5 ms. The volume fraction of ethanol obtained after the system approached this apparent steady state is shown in Figure 5.5, which mirrors the simulation domain for visualization purposes. The formation of a thin cone film of ethanol can be clearly seen. Furthermore, the cone angle is well defined.

It is important to emphasize, however, that while film thickness and cone half-angle can be extracted with accuracy from the simulation, droplet size and breakup phenomena are not precise. To model film instability, primary breakup and secondary breakup, non-axisymmetric effects need to be taken into consideration and thus, a much more expansive 3D simulation must be carried out.

Figure 5.5 – Volume Fraction of Ethanol inside the pressure-swirl atomizer

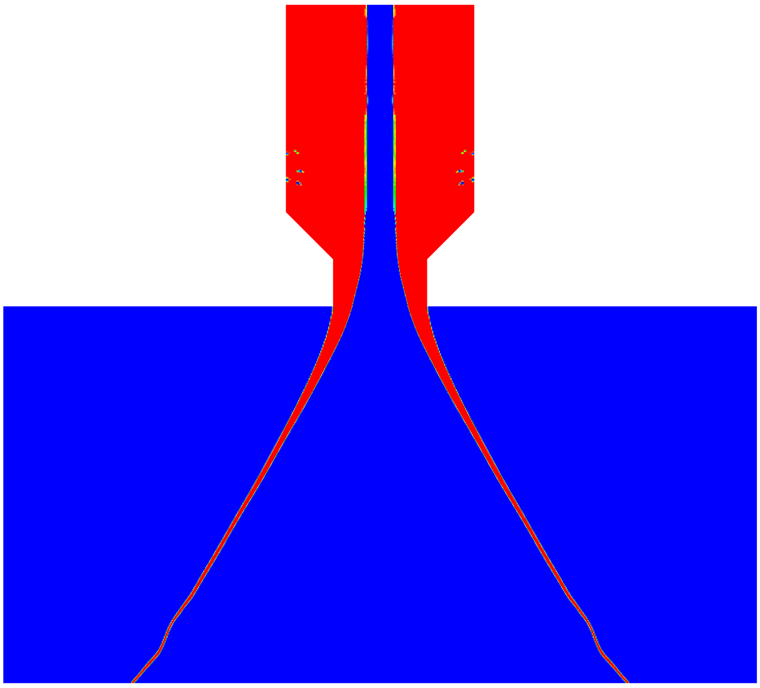

Source: Produced by the authors Ceotto & Tavares

The spray cone half-angle obtained was approximately 30°, in contrast with the 41° predicted by the analytical model. Furthermore, the film thickness at the orifice exit was approximately 0.502 mm, which is very close to the expected 0.495 mm. Total inlet pressure simulated was 48.2 bar, which results in a discharge coefficient of approximately 0.5026, versus 0.5067. Therefore, a large deviation was observed only for the spray half-cone angle. This discrepancy is probably due to viscous effects on the numerical simulation, which tend to decrease the swirl velocity, and hence the cone angle. Table 5.3 summarises the comparison between the analytical model and the VOF simulation.

Therefore, a good agreement between the analytical model and the VOF model was obtained, specially considering the simplicity of the analytical model when compared to the numerical simulation employed.

Table 5.3 – Comparison between predictions of the analytical model and the VOF simulation

Model	Analytical	VOF Simulation	Deviation
Discharge coefficient	0.5067	0.5026	0.8%
Film thickness (mm)	0.495	0.502	1.4%
Spray cone half-angle (degree)	40.1	30	25%
Total inlet pressure (bar)	47.4	48.2	1.7%

5.3.4 THREE-DIMENSIONAL SIMULATIONS USING VOF

As previously mentioned, two-dimensional axisymmetric simulations can accurately predict the cone half-angle and injector discharge coefficient. However, the flow instabilities which cause the formation of the droplets are inherently three-dimensional. Thus, the cone sheet primary breakup and droplet formation can only by modeled in a 3D environment. This is specially important to determine the position in which droplets form, as well as their Sauter Mean Diameter distribution.

With this in mind, the axisymmetric model was used to create a body of revolution. However, the 4 sided symmetry of the injector, which has four inlets was exploited. Thus only one-fourth of the body was considered for the simulation. Furthermore, the exact same numerical settings as in the two-dimensional simulation were used.

The preliminary steady-state ethanol free-surface is presented in Figure 5.6. The cone angle agrees well with the axisymmetric simulation, however, breakup instabilities and droplet size are still unreliable. A finer mesh is needed and will be used to improve this result in future work, when powerful computational infrastructure is available.

Figure 5.6 – Discharge coefficient as a function of injector cylinder length.

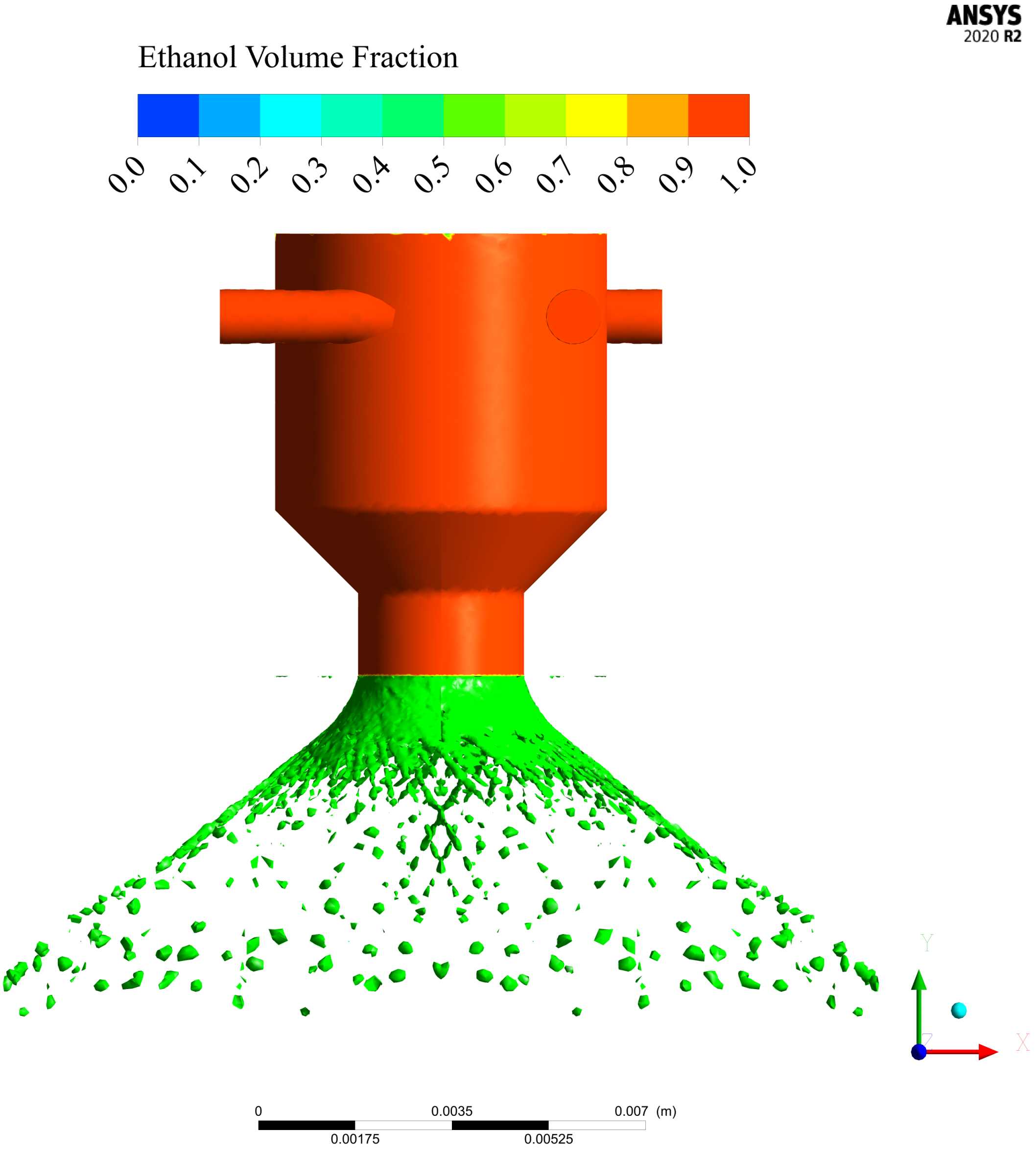

Source: Produced by the authors Ceotto & Tavares

6 NITROUS OXIDE INJECTOR

The analysis and design of the nitrous oxide injector started very similar to the ethanol injector. Since nitrous oxide will be in a saturated liquid state inside the oxidizer tank, the initial plan was to also employ a pressure-swirl atomizer.

Recently, however, preliminary CFD simulations have shown that it is very likely that the nitrous oxide will flash-boil still inside the injector. This greatly changes how the injector works since the vaporized nitrous oxide will mix with the air core, preventing its formation and greatly modifying the discharge coefficient.

Furthermore, the current analytical and numerical methodologies fail under this scenario, rendering them useless for the design of the nitrous oxide injector.

In fact, flash-boiling will most certainly affect any injector, even simple ones such as a single thick orifice plate. As mentioned in the literature review, flash-boiling must be taken into account to guarantee a correct design of the nitrous oxide injector.

6.1 NON-HOMOGENEOUS NON-EQUILIBRIUM (NHNE) ANALYTICAL MODEL

Despite these challenges, considerable effort from the scientific community has been put into developing trustworthy analytical models, which can be used in the preliminary phase of design. Along with experimental data, these models can accurately predict, up to an extent, the mass flow rate across a nitrous oxide injector. An example of such model is the one presented by (Dyer et al., 2007), later corrected by (Solomon, 2011). The total mass flow rate across the injector is defined as a balance between the mass flow rate considering single incompressible fluid ($\dot{m}_{SPI}$) and the mass flow rate considering thermal equilibrium between liquid and vapour phase ($\dot{m}_{HEM}$). It is written in the following fashion:

$$\dot{m} = \frac{k}{1+k}\dot{m}_{SPI} + \frac{1}{1+k}\dot{m}_{HEM} \tag{6.1}$$

The mass flow rate $m_{\dot{H}EM}$ corresponds to the Homogeneous Equilibrium Model, which takes into account the critical downstream pressure, where the flow becomes "choked", i.e. mass flow rate reaches a maximum value. It is defined as:

$$\dot{m}_{HEM} = C_d A \rho_2 \sqrt{2\left(h_1 - h_2\right)} \tag{6.2}$$

Where h_1 and h_2 are the upstream and downstream values of enthalpy for the nitrous oxide, respectively, considering a vapor fraction-weighted average (or vapor quality-weighted average). This fraction (or quality) is computed by assuming isentropic flow across the injector. However, $m_{\dot{H}EM}$ is not sufficient to describe the flow, because thermodynamic equilibrium might not be attained since liquids can exist below their vapor pressure if no nucleation sites are available for bubble initiation (Dyer et al., 2007). Therefore, the mass flow rate for incompressible liquid $\dot{m}_{SPI}$, given by equation 4.19, must be considered. The balance between the two is ensured by the parameter k, which is a ratio between bubble growth time τ_b and residence time τ_r of the liquid inside the injector, as follows:

$$k = \frac{\tau_b}{\tau_r} = \sqrt{\frac{P_1 - P_2}{P_v - P_2}} \tag{6.3}$$

Where P_1 and P_2 are the nitrous oxide upstream and downstream pressures, respectively, and P_v is its vapour pressure. It can be inferred that, if the flow spends little time inside the injector and bubbles grow quickly, a thermodynamic equilibrium model is not feasible. In this case, k gets big, and thus the mass flow rate term $m_{\dot{H}EM}$ becomes negligible, as expected.

Nevertheless, this model does not account for the ratio between length and diameter of the the orifice (L/D). As this ratio increases, the flow has more time to reach thermodynamic equilibrium, and therefore the Homogeneous Equilibrium Model dictates the mass flow rate, as shown by (Henry and Fauske, 1971). Hence one should be careful when designing injectors with high or low L/D ratios using the aforementioned model.

6.2 ANALYSES AND RESULTS

A nonimpinging (or shower head) injector was chosen for the nitrous oxide since good agreement between the proposed model and experimental data was found by (Dyer et al., 2007) for simple orifice injectors.

Following the methodology discussed in section 6.1, assuming all orifices have diameter of 1.5 mm and taking C_d as 0.66 from (Dyer et al., 2007) for this orifice size, it was possible to compute the number of orifices required to attain the desired mass flow rate: ten. CoolProp (Bell et al., 2014) was used for retrieving nitrous oxide properties.

Table 6.1 – Parameters of the nitrous oxide injector

Parameter	Value	Unit
Discharge coefficient	0.66	-
Orifice diameter	1.5	[mm]
Number of orifices	10	-

7 COMBUSTION MODELING

Inside the combustion chamber, ethanol droplets will mix with gaseous nitrous oxide due to flash boiling. The high temperature ambient will cause the droplets to vaporize. Ethanol vapor then reacts with nitrous oxide generating heat. When designing a combustion chamber, two objectives must be considered: it is crucial that almost every droplet fully vaporizes before reaching the nozzle, however, a significant proportion of them should not vaporize too close to the injector plate, since it is not cooled and could melt if intense combustion takes place near its surface (Spalding, 1959). This balance can be attained by selecting a combination of combustion chamber diameter and length which vaporizes a droplet of average diameter near the center of the chamber.

Therefore, in order to conduct a preliminary design of a rocket combustion chamber, knowledge about droplet vaporization, fuel-oxidizer mixing and combustion is needed. While CFD and even DNS are increasingly more relevant for combustion chamber design, the computational infrastructure available to the authors made their use impractical considering the scope and duration of this work. However, simplified zero-dimensional and one-dimensional models are sufficient to compute a suitable chamber diameter-length combination (Belal, Makled, and Al-Sanabawy, 2019). These models involve algebraic and ordinary differential equations, making them computationally inexpensive, which allows for faster design iterations, parametric studies and design optimization.

Before theses models and their results are shown, the reaction mechanisms and thermodynamic data needed for these will be presented. Then, a one-dimensional model of vaporization-controlled combustion is used to predict ethanol droplets lifetime. To conclude the combustion model, the vaporization-controlled reactor is combined with three plug-flow reactors (PFR) to estimate the evolution of mass fractions and gas temperature along the combustion chamber and nozzle.

7.1 REACTION MECHANISM AND THERMODYNAMIC DATA

While experimental studies on combustion characteristics of ethanol, C_2H_5OH, and nitrous oxide, N_2O, mixture have been conducted (Lee, Son, and Koo, 2014), no chemical reaction mechanism has been created and validate for such fuel-oxidizer pair. Since a thorough mechanism investigation is out of scope for this project, an alternative is to combine reaction mechanisms used for ethanol-air combustion (Marinov, 1999; Saxena and Williams, 2007; Cancino et al., 2010) with nitrous oxide decomposition mechanisms (MONAT, HANSON, and KRUGER, 1977). Another option would be to add an ethanol sub-mechanism into a hydrocarbon combustion mechanism which already contains nitrous oxide and related species, such as (Smith et al., 2000), which has already been used when nitrous oxide was the oxidizer (Wang, Ma, and Shen, 2020), or (Mével et al., 2009), which proposes a mechanism for hydrogen-nitrous oxide combustion. To evaluate the best options, three new mechanisms for ethanol-nitrous oxide combustion were created.

The first one is based on the San Diego Mechanism (Saxena and Williams, 2007), which is used for combustion simulations of several hydrocarbons, including ethanol. Since the San Diego Mechanism also provides a sub-mechanism for nitrogen species which include nitrous oxide, this sub-mechanism is combined with the original mechanism to achieve the desired result. In total, the complete mechanism has 68 species and 311 reactions, with 45 reactions related to the nitrogen sub-mechanism.

The second mechanism created combines (Marinov, 1999) as an ethanol mechanism with (Mével et al., 2009) which serves as a sub mechanism for nitrous-oxide and other nitrogen base compounds. In total, this mechanism contains 93 species and 664 reactions, with a total of 281 reaction related to the nitrogen sub-mechanism, which is significantly more than the first proposed mechanism.

The last mechanism is also based on (Marinov, 1999) for the ethanol mechanism. However, nitrous-oxide decomposition is based the nitrogen sub-mechanism from (Smith et al., 2000), which includes not only nitrogen and oxygen equations but also nitrogen-carbon and nitrogen-hydrogen. In total, this mechanism contains 75 species and 494 reactions, with only 18 reactions related to the nitrogen sub-mechanism.

Table 7.1 provides a summary comparing the proposed mechanisms. In general, all three reaction mechanisms come from different bases. All mechanism files can be found at (Ceotto, Dias, and Tavares, 2020). To compare them and attempt to analyse their validity, the ignition delay in an ideal gas constant-pressure fixed-mass reactor is calculated. A constant pressure reactor is chosen so that the rocket's combustion chamber pressure can be used in this analysis.

Table 7.1 – Proposed mechanism comparison.

Identification	**San Diego**	**Marinov + Mevel**	**Marinov + GRI**
Hydrocarbon mechanism	San Diego	Marinov	Marinov
NOX mechanism	San Diego	Extracted from Mevel	Extracted from GRI 3.0
Species	68	93	75
Reactions	311	664	494
Ignition delay	$9.2\,\mu$s	$4.6\,\mu$s	$6.5\,\mu$s

The reactor considers a completely homogeneous systems, meaning that a single value of each variable is needed to describe the entire volume of the reactor. The governing equations of this reactor (Turns, 1996) are ordinary differential equations which describe the evolution of reactor temperature, T, and species mass fractions, $[X_i]$:

$$\frac{\mathrm{d}T}{\mathrm{d}t} = \frac{\sum_i \left(\bar{h}_i \dot{\omega}_i\right)}{\sum_i \left([X_i]\, \bar{c}_{p,i}\right)}, \tag{7.1}$$

$$\frac{\mathrm{d}\,[X_i]}{\mathrm{d}t} = \dot{\omega}_i - [X_i] \left[\frac{\sum \dot{\omega}_i}{\sum_j [X_j]} + \frac{1}{T}\frac{\mathrm{d}T}{\mathrm{d}t}\right], \tag{7.2}$$

where $\bar{h}_i$ is the molar enthalpy and $\dot{\omega}_i$ is the molar production rate of species . The latter is given by the reaction mechanisms as a function of species concentration. The molar heat capacity of the mixture is given by $\sum_i \left([X_i]\, \bar{c}_{p,i}\right)$.

This forms an initial-value problem which can be integrated in time to result in the evolution of an initially premixed mixture of fuel and oxidizer. The reactor was simulated using Cantera (Goodwin et al., 2018) and all three mechanisms considered an initially stoichiometric mixture at 15 bar and 1500 K. The temperature evolution for each mechanism is shown in Figure 7.1, while 7.1 summarizes the results. Even though the results are different, all three mechanisms resulted in an ignition delay of the order of 10^{-5}s. This and the fact that these values are reasonable for ignition delays when nitrous oxide is used as the oxidizer (Mével et al., 2009) supports the mechanisms proposed. The authors choose to continue with the *Marinov + Mevel* mechanism for the rest of the simulations since it contains a more detailed model of nitrous-oxide related reactions. Furthermore, its large size in terms of number of species and reactions is not an issue here since the model will only be used for zero-dimensional and one-dimensional simulations.

Thermodynamic and transport properties will also be necessary for the following analyses. These come directly from the reaction mechanisms used: San Diego, Marinov, Mevel and GRI 3.0. As species are considered to be in the gas phase. Liquid and phase-change

Figure 7.1 – Ignition delay for the proposed mechanisms considering a constant pressure reactor with an initial stoichiometric mixture of ethanol and nitrous oxide at 1500 K.

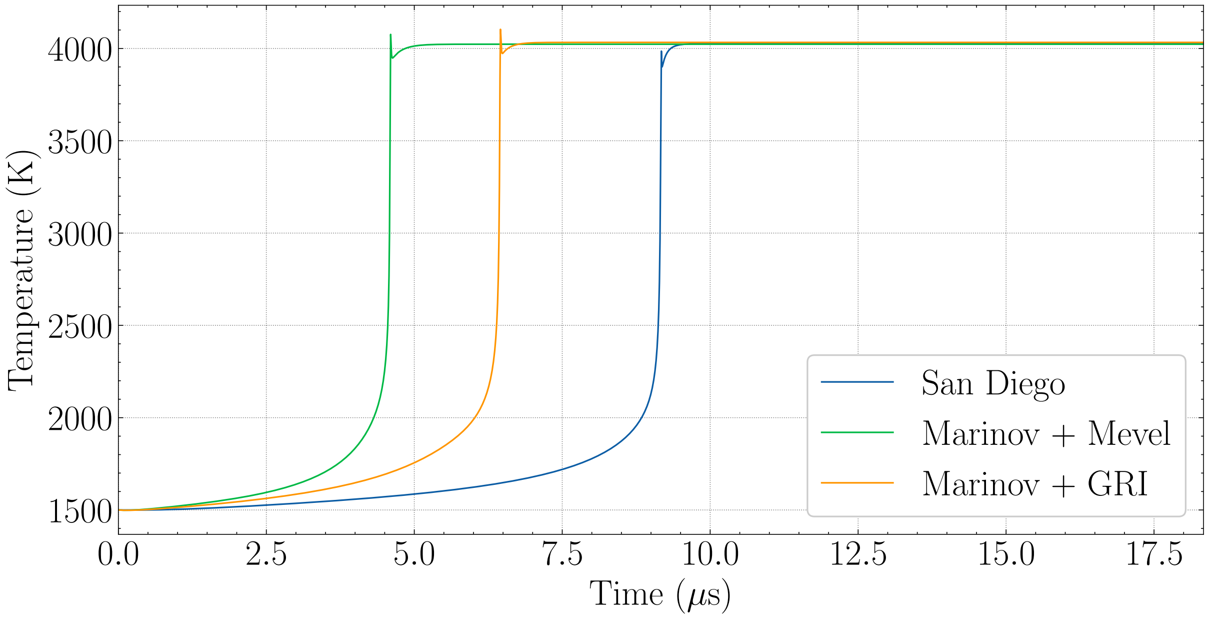

Source: Produced by the authors Ceotto & Tavares

properties are only needed for ethanol, since its droplets have a considerable lifetime as will be shown in the next section. Such properties used here come from (Bell et al., 2014).

A important thermodynamic property which will be used in the models to come is the equilibrium enthalpy of the combustion gases, as a function of temperature, pressure and equivalence ratio. Using the thermodynamic properties specified and Cantera, equilibrium calculations were done to produce the graph presented in Figure 7.2.

7.2 VAPORIZATION-CONTROLLED PLUG FLOW REACTOR

Both ethanol and nitrous oxide are stored as liquid before being injected in the combustion chamber as described previously. However, due to flash boiling, the vaporization of nitrous oxide is expected to be significantly faster than vaporization of ethanol droplets. In turn, ethanol droplets are expected to have a lifetime orders of magnitudes greater than the characteristic combustion time scale, which should have a similar order of magnitude as the ignition delay presented previously. In this section, a one-dimensional reactor will be modeled inspired by (Turns, 1996), (Spalding, 1959) and (Belal, Makled, and Al-Sanabawy, 2019) to verify these hypothesis and calculate the lifetime of ethanol droplets. These reactor will also be used in a reactor network in subsequent sections.

Figure 7.2 –
Enthalpy contour for a nitrous oxide and ethanol mixture considering constant temperature and pressure equilibrium for a range of temperatures and equivalence ratios. Pressure is kept constant at 35 bar.

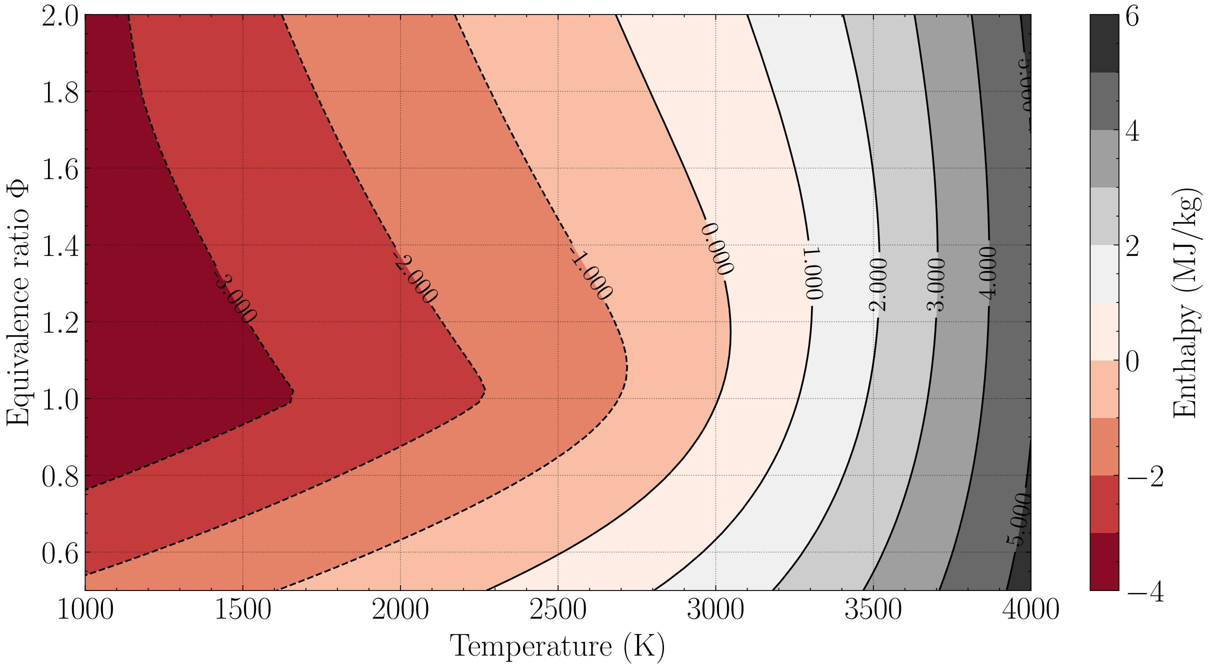

Source: Produced by the authors Ceotto & Tavares

The model consists in the following simplifying assumption:

- One-dimensional flow, meaning every variable will have an uniform distribution along the radial direction of the combustion chamber, changing only in the axial direction.
- No circulation or back-mixing exists.
- Diffusion is neglected, even though axial gradients are not.
- Pressure is constant along the reactor, equal to the combustion chamber pressure.
- The flow contains two phases: liquid ethanol droplets at a constant temperature equal to their boiling temperature and a gas phase comprising nitrous oxide and combustion products.
- Ethanol droplets are injected with a single diameter, equal to the Sauter Mean Diameter. Their initial velocities is equal to the axial velocity of ethanol at the injector outlet face.

- Combustion is assumed to happen significantly faster than the droplets lifetime. This means that infinite rate chemistry will be considered and thus equilibrium will be used to calculate enthalpy variations and mixture composition.
- Droplet vaporization can be modeled assuming unitary Lewis number, without convective effects.

Given these assumptions, the model considered here tracks the following variables along the combustion chamber axis, x:

- $D(x)$, droplet diameter;
- $\dot{m}_g(x)$, gas phase mass flow rate;
- $\dot{m}_l(x)$, liquid ethanol flow rate;
- Φ_g, equivalence ratio;
- $T_g(x)$, gas phase temperature;
- $v_d(x)$, droplet velocity;
- $v_g(x)$, gas phase velocity;

As such, six differential equations are needed to solve them and one additional algebraic equation is needed for $v_g(x)$. The first differential equation describes the evolution of the droplet diameter $D(x)$ and is given by the well known droplet diameter squared equation (Turns, 1996) transformed from time coordinates to space coordinates by the droplet velocity $v_d(x)$:

$$\frac{\mathrm{d}D^2}{\mathrm{d}x} = -\frac{K}{v_d(x)}, \qquad K = \frac{8k_g}{\rho_l c_{p,v}} \ln\left(1 + \frac{c_{p,v}(T_\infty - T_{boil})}{h_{fg}}\right), \tag{7.3}$$

where $c_{p,v}$ is the constant pressure specific heat of ethanol vapor calculated at $\bar{T} = \mathrm{mean}(T_\infty, T_{boil})$ and k_g is the its thermal conductivity, calculated as $k_g = 0.4k_v(\bar{T}) + 0.6k_\infty(\bar{T})$. The liquid density is denoted by ρ_l and the heat of vaporization by h_{fg}.

While the droplet lifetime is not needed in the model, it is important to verify the model's assumption. It is given by (Turns, 1996):

$$t_d = \frac{D^2(0)}{K} \tag{7.4}$$

Once dD^2/dx is known, the axial derivative of the liquid flow rate can be easily calculated, since it corresponds to the evaporation rate:

$$\frac{\mathrm{d}\dot{m}_l}{\mathrm{d}x} = \frac{\pi}{4}\dot{N}\rho_l D \frac{\mathrm{d}D^2}{\mathrm{d}x}, \tag{7.5}$$

where $\dot{N}$ is the number of ethanol droplets injected per unit time. Following conservation of mass, knowing that the combustion chamber has no other inlets besides at $x = 0$, it is possible to calculate the axial derivative of $\dot{m}_g$:

$$\frac{\mathrm{d}\dot{m}_g}{\mathrm{d}x} = -\frac{\mathrm{d}\dot{m}_l}{\mathrm{d}x} \tag{7.6}$$

The equivalence ratio follows directly from these mass flow rates (Turns, 1996):

$$\frac{\mathrm{d}\Phi(x)}{\mathrm{d}x} = \frac{1}{(F/O)_{\phi=1}} \frac{\mathrm{d}\dot{m}_g}{\mathrm{d}x} \frac{1}{\dot{m}_g(0)}, \tag{7.7}$$

where $(F/O)_{\phi=1}$ is the stoichiometric fuel to oxidizer ratio.

The temperature differential equation comes from the energy equation considering infinite rate chemistry:

$$\frac{\mathrm{d}T_g}{\mathrm{d}x} = \left(\frac{h_g - h_l}{\dot{m}_g}\frac{\mathrm{d}\dot{m}_g}{\mathrm{d}x} - \frac{\partial h_g}{\partial \Phi}\frac{\mathrm{d}\Phi}{\mathrm{d}x}\right)\left(\frac{\partial h_g}{\partial T}\right)^{-1}. \tag{7.8}$$

Here, $\frac{\partial h_g}{\partial \Phi}$ and $\frac{\partial h_g}{\partial T}$ are calculated by evaluating derivatives of the plot shown in Figure 7.2.

And finally, the last differential equation of the model consists in the dynamic model of the liquid droplets, whose acceleration is determined by their mass and drag coefficients:

$$\frac{\mathrm{d}v_d}{\mathrm{d}x} = \frac{3C_D\rho_g v_{\mathrm{rel}}^2}{4\rho_l v_d D}, \tag{7.9}$$

where the drag coefficient C_D is calculated by (Turns, 1996):

$$C_D \approx \frac{24}{Re_{D,\mathrm{rel}}} + \frac{6}{1+\sqrt{Re_{D,\mathrm{rel}}}} + 0.4, \tag{7.10}$$

while the subscript rel represents a relative quantity with respect to the velocity of the gas v_g.

This brings the model to its last equation, an algebraic equation for v_g which comes from the definition of the mass flow rate:

$$v_g = \frac{\dot{m}_g R_u T_g}{MW_g P A}, \tag{7.11}$$

where P is the chamber pressure, A its cross sectional area, MW_g the molecular weight of the gas phase and R_u the universal gas constant.

This model is, mathematically speaking, an initial value problem. Giving initial conditions, at $x = 0$, it can be integrated in x until axial steady state has been reached. The differential equations have been implemented in Python and solved using SciPy's integration routines. The code can be accessed in (Ceotto, Dias, and Tavares, 2020).

As a result, the droplet lifetime calculate by the model is:

$$t_d = 834\,\mu\text{s} \tag{7.12}$$

This is three orders of magnitude larger than the characteristic reaction time, demonstrating the validity of the model.

7.3 VARYING-AREA PLUG FLOW REACTOR

Varying-Area Plug Flow Reactors are a standard section of combustion textbooks nowadays (Turns, 1996). In a rocket's combustion chamber design, they can be used to model reacting flow along the section of the camber which does not contain droplets, as well as along the rocket's nozzle. The model is also one-dimensional and is based on the following hypothesis:

- Mixing in the axial direction of the combustion chamber can be neglected. No molecular or turbulent diffusion is considered.
- Friction-less, steady-state, steady flow.
- Gaseous mixture has ideal-gas behavior.

Considering this, the flow can be fully characterized by the knowledge of its density, ρ_g, temperature T_g and composition, expressed in terms of species mass fraction Y_i. From these, remaining important variables can be readily calculated employing algebraic relations, such as pressure P (using the Ideal-Gas law), and flow velocity v_g using a known and constant mass flow rate. This means, the system is fully defined by the following differential equations (Turns, 1996):

$$\frac{\mathrm{d}\rho_g}{\mathrm{d}x} = \frac{\left(1 - \frac{R_u}{c_p MW_\text{mix}}\right)\rho_g^2 v_g^2 \left(\frac{1}{A}\frac{\mathrm{d}A}{\mathrm{d}x}\right) + \frac{\rho_g R_u}{v_g c_p MW_\text{mix}} \sum_{i=1}^{N} MW_i \dot{\omega}_i \left(h_i - \frac{MW_\text{mix}}{MW_i} c_p T_g\right)}{P\left(1 + \frac{v_g^2}{c_p T}\right) - \rho_g v_g^2} \tag{7.13}$$

$$\frac{\mathrm{d}T_g}{\mathrm{d}x} = \frac{v_g^2}{\rho_g c_p}\frac{\mathrm{d}\rho_g}{\mathrm{d}x} + \frac{v_g^2}{c_p}\left(\frac{1}{A}\frac{\mathrm{d}A}{\mathrm{d}x}\right) - \frac{1}{v_g \rho_g c_p}\sum_{i=1}^{N} h_i \dot{\omega}_i MW_i + \frac{\dot{q}'}{c_p \rho_g} \tag{7.14}$$

$$\frac{\mathrm{d}Y_i}{\mathrm{d}x} = \frac{\dot{\omega}_i MW_i}{\rho_g v_g} \tag{7.15}$$

Where c_p indicates the constant pressure specific heat of the gaseous mixture, $\dot{\omega}_i$ denotes the net production rate of the i-*th* species, which can be readily calculated given the reaction mechanisms described above and the mass fraction of each species. MW represents molecular weight while R_u is the universal gas constant. Furthermore, these equations also consider the cross-sectional area variation typical of rocket nozzles. The cross sectional area at each axial position x is denoted by $A(x)$. Possible heat exchange is also modeled by the heat transfer per unit length term, $\dot{q}'$. In case of rockets, regenerative cooling remove a significant heat from the combustion chamber and nozzle flow, therefore, making such inclusion in the model important.

Equations 7.13, 7.14, and 7.15 are initialized using specified values of $\rho_g(x)$, $T_g(x)$ and $Y_i(x)$ at $x = x_0$.

7.4 REACTOR NETWORK MODEL

Both one-dimensional reactors described above can be readily arranged in series to form a chemical reactor network which represents the basic characteristics of a rocket's combustion chamber and nozzle in steady-state. To do so, a typical combustion chamber - nozzle combination is split into four parts as shown in Figure 7.3:

- a vaporization-controlled reactor, starting at the injector plate and ending when droplet radius reaches zero;
- a constant-area plug flow reactor, which models the remaining of the combustion chamber;
- a converging plug flow reactor, which models the converging section of the nozzle and ends at Mach 1;
- a diverging plug flow reactor for the the diverging section of the nozzle.

While the second and third reactors could be merged, it is more efficient to solve them separately since equations 7.13, 7.14, and 7.15 can be simplified for a constant-area reactor. On the other hand, the third and fourth reactor, which models the nozzle, is usually divided to prevent singularities which may occur numerically in equations 7.13, 7.14 and 7.15 at Mach 1. Each reactor is solved in sequence and fed as starting condition the end state of the previous reactor. In this case, the coordinate system is such that the combustion chamber starts at $x = --275\,\mathrm{mm}$, and the nozzle throat is conveniently

Figure 7.3 – Reactor Network Model for a combustion chamber - nozzle system.

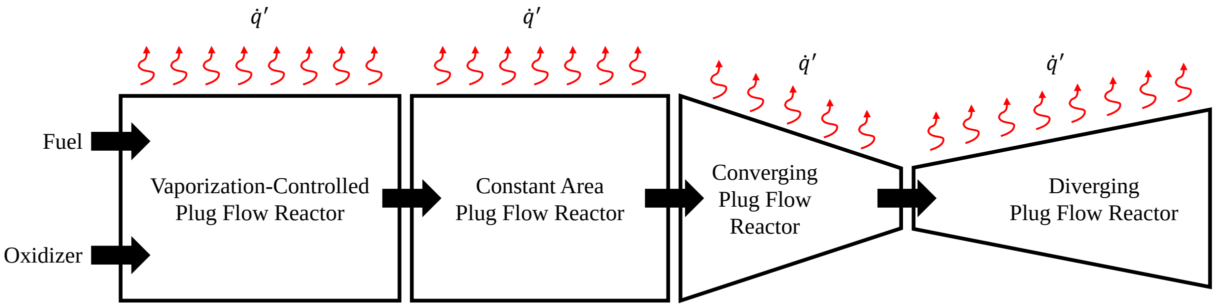

Source: Produced by the authors Ceotto & Tavares

at $x = -0\,\text{mm}$. The vaporization-controlled reactor starts with the following initial conditions at $x = -275\,\text{mm}$:

- Droplet initial diameter (SMD): $D_0 = 40.0\,\mu\text{m}$;
- Droplet initial velocity: $v_{d,0} = 93.75\,\text{m/s}$
- Liquid ethanol mass flow rate: $m_{l,0} = 0.314\,\text{kg/s}$
- Gas mass flow rate (initially only nitrous oxide): $m_g = 1.103\,\text{kg/s}$
- Initial equivalence ratio: $\Phi = 0$.

Such conditions generates the results shown in Figure 7.4. The first critical data which can be observed from the graph is the position where the droplet radius goes to zero, meaning that droplets have completely evaporated. This occurs at $x - x_0 = 91.5\,\text{mm}$ after the injector plate, which shows that the selected combustion chamber length of $L = 200\,\text{mm}$ would sufficient for complete droplet evaporation and combustion. However, it is important to remember the limitations of the vaporization-controlled reactor: all droplets are assumed to have the same diameter. Since this is not the case, some droplets will have an initial diameter larger than the predicted SMD and will, thus, evaporate only later in the combustion chamber, approaching the nozzle.

The graph in Figure 7.4 also shows how the temperature peaks near $x - x_0 = 20\,\text{mm}$. This occurs when the equivalence ratio of the mixture becomes one. For larger values of x, more ethanol evaporates increasing the equivalence ratio and creating a rich mixture. Therefore, the temperature starts to drop again.

Approaching the nozzle, compressible flow becomes more significant and the typical acceleration provided by choked nozzles can be observed. Since the nozzle is not the main concern of this work, no further analysis will be carried out here. However, it must be emphasized that the reactor network implemented is capable of analyzing nozzles and producing relevant results for nozzle design considering reactive flow. This differs from simplified models which generally assume equilibrium or frozen flow (Gordon and McBride, 1994).

Figure 7.4 – Resulting evolution of main variables in the Reactor Network developed. r_* indicates throat radius, while T_{ad} denotes the stoichiometric adiabatic flame temperature and ρ_0 is the initial density, not to be confused with total density.

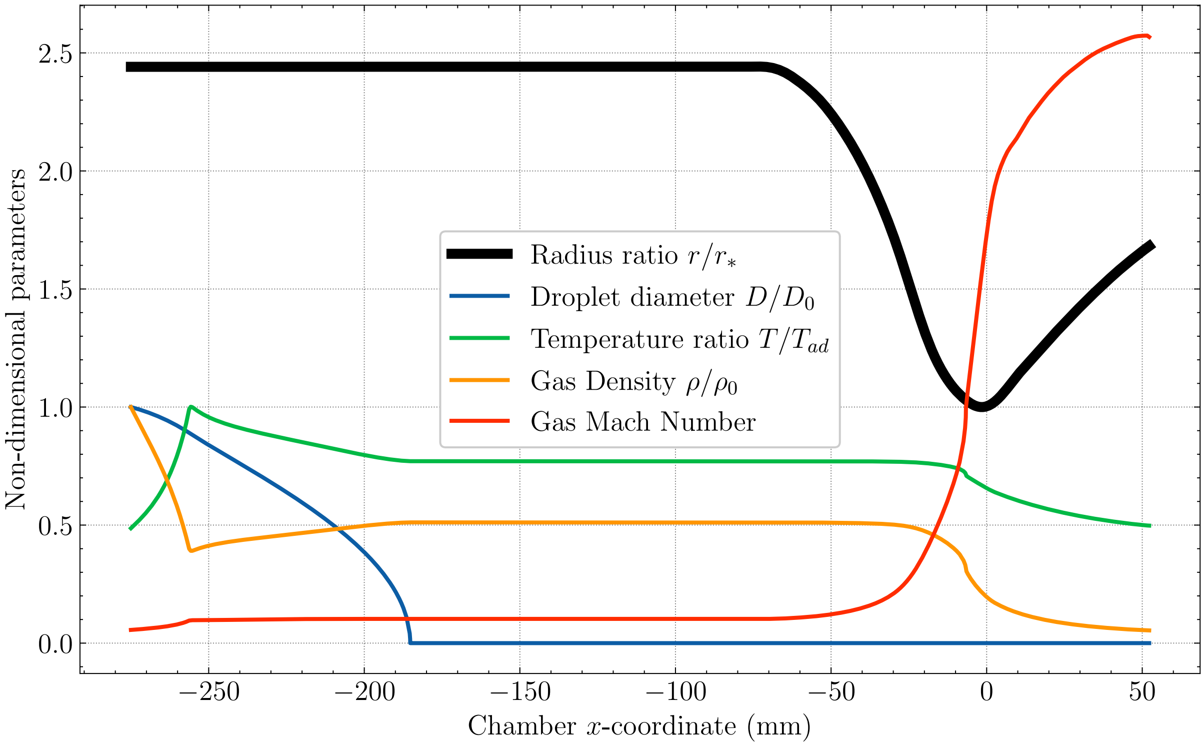

Source: Produced by the authors Ceotto & Tavares

8 COMBUSTION INSTABILITY

The understanding and forecast of combustion instabilities are of utmost importance in the development of liquid rocket engines. If not properly assessed, they can lead to severe pressure vibration forces, which can blow the engine apart. In order to address the problem, engineers must properly design combustion chamber, injection systems and feed lines, among others, adding (or removing) features with the goal of preventing instabilities from occurring.

According to (Sutton and Biblarz, 2016), combustion instabilities can be divided into three types, according to the respective frequency range: the first one, deemed chugging, is related to possible pressure and mass flow disturbances on the propellant feed lines, within the 10-400 Hz frequency range. For instance, in the event of a slight increase on the rocket thrust (and therefore of the vehicle's compression), there will be a sudden rise on the propellant upstream pressure, which in turn will lead to a higher mass flow rate to the combustion chamber, and thus to a bump in the thrust. This dynamic produces a longitudinal vibration motion, which can turn out to be unstable if there is a match between the resonance frequencies of the feed lines and the combustion chamber. This combustion instability is called *pogo* phenomenon, after the resemblance to the bouncing of the pogo stick, a children's toy.

Buzzing, the intermediate one, within the 400-1000 Hz frequency range, usually does not lead to pressure fluctuation above $\pm 5\%$ of the mean chamber pressure, which would characterize a transition from a so-called smooth combustion to a unstable combustion. Caused by coupling between the combustion process and flow on the propellant feed system, it is therefore not a big concern.

Screeching (or screaming), on the other hand, is the most damaging type. Given its higher frequency range (above 1000 Hz), it is also the one that carries the most energy, capable of being utterly destructive in a matter of seconds. It has its roots in the combustion chamber alone, where pressure waves and the acoustical resonance properties may lead to unstable behaviour. This high-frequency instability manifests itself in acoustic longitudinal vibration modes (parallel to the combustion chamber axis) and transverse vibration modes (radial and tangential modes). Both are driven by energy from "acoustically stimulated variations in droplet vaporization and/or mixing and local detonations" (Sutton and Biblarz, 2016). Screeching is usually avoided by the use of acoustic absorbers, such as injector face baffles, which reduces coupling and amplification of gas dynamics forces, and acoustic cavities, which increase acoustical damping within the combustion chamber.

Given its possible (and sudden) catastrophic influence on engine operation, only screeching will receive a thorough investigation. The purpose of the present chapter is to give a brief overview on combustion phenomena that may lead to acoustic modes being self-excited, to derive the latter for the herein developed nitrous oxide and ethanol rocket engine and to present, discuss and propose a passive control technique. Results from a planned hot-fire test will reveal if the rocket is susceptible to combustion instability, and if so, which acoustic modes are unstable, which will lead to future work aiming at counteracting this issue.

8.1 ACOUSTIC COMBUSTION INSTABILITY MECHANISM

The mechanism that lead to acoustic combustion instability must foremost satisfy Rayleigh's criterion. It states that the rate of unsteady heat release must be in phase with pressure oscillations in order to vibration to be encouraged, i.e, to the amplitude of the pressure waves to grow. Also, the energy released from unsteady combustion must be grater than the energy dissipated across the system boundaries (Rayleigh, 1896).

The unsteady heat release is responsible for giving rise to acoustic perturbations (in the form of pressure waves), which travel along the combustion chamber until they are reflected at the boundary and come back towards the injector plate, possibly amplifying flame oscillations if with correct phasing, leading to instability growth (Bennewitz and Frederick, 2013).

Unsteady heat release is related to the processes in which the propellant interacts with the combustion chamber (such as injection, atomization, vaporization, mixing and combustion). These processes may excite acoustic modes (and vice versa) if their characteristic time is of the same order of magnitude as that of the modes, possibly leading to unstable behaviour.

Vaporization is usually considered to be the rate controlling process for combustion (in subcritical injection), as it tends to occurs more slowly in comparison with the aforementioned processes. As vaporization may occur due to boiling and/or evaporation, one of these process will be limiting. The characteristic time associated with boiling (a bulk phenomenon) is generally longer than the one associated with evaporation (a surface phenomenon); thus, boiling is the rate limiting process. Its characteristic time is on the order of 10^{-3} seconds, close to that of acoustic oscillations. Chemical time (proportional to chemical kinetic rates of reaction) in fuel rich combustion is also around this order of magnitude, thus making combustion itself a possible driver of instability by interacting with acoustic modes (Bennewitz and Frederick, 2013).

8.2 ACOUSTIC THEORY

The following mathematical formulation aims to describe the three-dimensional acoustic wave propagation in a cylindrical cavity (such as a rocket combustion chamber). It assumes isentropic flow, very small pressure disturbances, that the gas mixture from the products of combustion behaves like one continuous compressible medium, and can be found on (Zucrow and Hoffman, 1977).

The continuity, momentum and speed-of-sound equation can be written, respectively, as follows:

$$\frac{\partial \widetilde{\rho}}{\partial t} + \nabla . \left(\widetilde{\rho} \vec{V} \right) = 0 \tag{8.1}$$

$$\widetilde{\rho} \left(\frac{\partial \vec{V}}{\partial t} + \vec{V} . \nabla \vec{V} \right) + \nabla \widetilde{p} = 0 \tag{8.2}$$

$$\frac{D\widetilde{p}}{Dt} - \widetilde{a}^2 \frac{D\widetilde{\rho}}{Dt} = 0 \tag{8.3}$$

Combining equations 8.1 and 8.3 yields:

$$\widetilde{\rho} \widetilde{a}^2 \nabla . \vec{V} + \frac{D\widetilde{p}}{Dt} = 0 \tag{8.4}$$

Where the letters with the *tilde* above reference a dimensional flow property, whereas letter without it reference a perturbation or a disturbance of the respective flow property. Assuming the free-stream velocities (u, v and w, on the x, y and z directions, respectively) to be null:

$$\widetilde{u} = u \tag{8.5}$$

$$\widetilde{v} = v \tag{8.6}$$

$$\widetilde{w} = w \tag{8.7}$$

$$\widetilde{p} = p_\infty + p \tag{8.8}$$

$$\widetilde{\rho} = \rho_\infty + \rho \tag{8.9}$$

$$\widetilde{a} = a_\infty + a \tag{8.10}$$

Where p is the pressure, ρ is the density, a is the local speed of sound and the subscript ∞ refers to the free-stream value of the variable. The disturbances are taken as much smaller than the corresponding undisturbed values.

Applying the above definitions and assumptions to equations 8.4 and 8.2 leads, respectively, to:

$$\rho_\infty a_\infty^2 \left(\frac{\partial u}{\partial x} + \frac{\partial v}{\partial y} + \frac{\partial w}{\partial z}\right) + \frac{\partial p}{\partial t} = 0 \tag{8.11}$$

$$\rho_\infty \frac{\partial u}{\partial t} + \frac{\partial p}{\partial x} = 0 \tag{8.12}$$

$$\rho_\infty \frac{\partial v}{\partial t} + \frac{\partial p}{\partial y} = 0 \tag{8.13}$$

$$\rho_\infty \frac{\partial w}{\partial t} + \frac{\partial p}{\partial z} = 0 \tag{8.14}$$

Assuming second derivatives are continuous, differentiating equations 8.11, 8.12, 8.13 and 8.14 by t,x,y and z, respectively, and eliminating the partial derivatives $\frac{\partial u}{\partial x \partial t}$, $\frac{\partial v}{\partial y \partial t}$ and $\frac{\partial w}{\partial z \partial t}$ yields the three-dimensional wave equation:

$$\frac{\partial^2 p}{\partial t^2} = a_\infty^2 \left(\frac{\partial^2 p}{\partial x^2} + \frac{\partial^2 p}{\partial y^2} + \frac{\partial^2 p}{\partial z^2}\right) = a_\infty^2 \nabla^2 p \tag{8.15}$$

Which is a linear equation for the propagation of a small pressure disturbance in a stationary gas, where ∇^2 denotes the Laplacian operator. Due to this linearity, the pressure field can be obtained through the superposition of different waves that may be propagating in the three-dimensional space. Therefore, the next logical step is to characterize the shapes and frequencies of these individual waves, through a modal analysis.

In a cylindrical coordinate system, the above equation may be rewritten as:

$$\frac{\partial^2 p}{\partial t^2} = a_\infty^2 \left(\frac{\partial^2 p}{\partial r^2} + \frac{1}{r}\frac{\partial p}{\partial r} + \frac{1}{r^2}\frac{\partial^2 p}{\partial \theta^2} + \frac{\partial^2 p}{\partial z^2}\right) \tag{8.16}$$

Where r refers to the radial distance, θ to the azimuth and z to the axial coordinate. This is the equation for which a general solution will be determined.

The method of separation of variables is used, with the pressure written as function of four independent complex-valued functions of the variables r,θ,z and t, as follows:

$$p\left(r,\theta,z,t\right)=R(r)\Theta(\theta)Z(z)T(t) \tag{8.17}$$

By substituting equation 8.17 into 8.16, dividing by $R\Theta ZT$ and using the prime superscript ()' to denote the derivative of a function with respect to its argument, one finds:

$$\frac{T"}{a_\infty^2 T}=\frac{Z"}{Z}+\frac{R"}{R}+\frac{1}{r}\frac{R'}{R}+\frac{1}{r^2}\frac{\Theta"}{\Theta} \tag{8.18}$$

Which leads to an equation with its left-hand side dependent only on t, while its right-hand side is dependent only on r, θ and z. Given the equality, both sides must be equal to some constant, such as $-\lambda^2$. Therefore the left-hand side can be written as:

$$T"+\lambda^2 a_\infty^2 T=0 \tag{8.19}$$

Likewise:

$$-\frac{Z"}{Z}=\frac{R"}{R}+\frac{1}{r}\frac{R'}{R}+\frac{1}{r^2}\frac{\Theta"}{\Theta}+\lambda^2 \tag{8.20}$$

Again, both sides must be equal to some constant, such as ϕ^2. Hence:

$$Z"+\phi^2 Z=0 \tag{8.21}$$

And:

$$\frac{R"}{R}+\frac{1}{r}\frac{R'}{R}+\frac{1}{r^2}\frac{\Theta"}{\Theta}=\phi^2-\lambda^2=-\sigma^2 \tag{8.22}$$

Therefore:

$$-\frac{\Theta"}{\Theta}=r^2\frac{R"}{R}+r\frac{R'}{R}+\sigma^2 r^2 \tag{8.23}$$

Once more, denoting γ^2 as the constant that is equal to each side of the above equation leads to:

$$\Theta"+\gamma^2\Theta=0 \tag{8.24}$$

And:

$$r^2R"+rR'+\left(\sigma^2r^2-\gamma^2\right)R=0 \tag{8.25}$$

As a result, the three-dimensional wave equation (8.16) has been replaced by four ordinary differential equations. The general solutions for the first three equations (8.19, 8.21 and 8.24, respectively) are shown below:

$$T(t)=G\exp(ia_\infty\lambda t)+H\exp(-ia_\infty\lambda t) \tag{8.26}$$

$$Z(z)=E\exp(i\phi z)+F\exp(-i\phi z) \tag{8.27}$$

$$\Theta = C\exp(i\gamma\theta) + D\exp(-i\gamma\theta) \tag{8.28}$$

Rewriting equation 8.25 yields:

$$r^2\frac{d^2R}{dr^2} + r\frac{dR}{dr} + \left(\sigma^2r^2 - n^2\right)R = 0 \tag{8.29}$$

Which is known as Bessel's differential equation. It can be solved by assuming R to be a power series of r, and this leads to two linearly independent solutions (if n is an integer): the first one is denoted $J_n(r)$ (Bessel function of the first kind), which is finite at $r = 0$, while the second one is denoted $Y_n(r)$ (Bessel function of the second kind), which is infinite at $r = 0$. Therefore, the solution of equation 8.25 is given by:

$$R(r) = AJ_n(\sigma r) + BY_n(\sigma r) \tag{8.30}$$

With the Bessel function of the first kind J_n being defined, for each fixed n, as:

$$J_n(\sigma r) = \sum_{m=0}^{+\infty} \frac{(-1)^m}{m!(n+m)!}\left(\frac{\sigma r}{2}\right)^{2m+n} \tag{8.31}$$

It is important to point out the relationship between the separation constants λ, ϕ and σ:

$$\lambda^2 = \phi^2 + \sigma^2 \tag{8.32}$$

The aforementioned parameters can be rewritten, with no loss of generality, as:

$$\lambda = \frac{\omega}{a_\infty} \tag{8.33}$$

$$\sigma = \frac{\alpha}{R} \tag{8.34}$$

$$\phi = \frac{\xi}{L} \tag{8.35}$$

Where ω is the frequency of the oscillations in the cavity, a_∞ is the acoustic speed in the undisturbed gas, α is a constant characteristic of the radial and tangential oscillations, R is the radius of the cylinder, ξ is a constant characteristic of the axial oscillations and L is the length of the cylinder. Thus, equation 8.32 becomes:

$$\frac{\omega^2}{a_\infty^2} = \frac{\alpha^2}{R^2} + \frac{\xi^2}{L^2} \tag{8.36}$$

The next step is to find the specific cylindrical solution, by applying appropriate initial and boundary conditions to the general solutions. The domain is assumed to be a hollow rigid cylinder, closed at both ends. Therefore:

- 1. At the walls, the velocity component normal to the boundary is null, which implies $v_r = 0$ at $r = R$ and $v_z = 0$ at $z = 0$ and $z = L$.
- 2. For all values of r, θ, z and t, the function $p(r, \theta, z, t)$ is finite.
- 3. The specific solution is periodic in θ with a period of 2π.

The first boundary condition must be imposed on the momentum equation 8.2, with respect to the r and z directions. For the r direction, the momentum equation is written as follows:

$$\widetilde{\rho}\left(\frac{\partial \widetilde{v}_r}{\partial t} + \widetilde{v}_r \frac{\partial \widetilde{v}_r}{\partial r} + \frac{\widetilde{v}_\theta}{r}\frac{\partial \widetilde{v}_r}{\partial \theta} - \frac{\widetilde{v}_\theta^2}{r} + \widetilde{v}_z \frac{\partial \widetilde{v}_r}{\partial z}\right) = -\frac{\partial \widetilde{p}}{\partial r} \tag{8.37}$$

Likewise, for the z direction:

$$\widetilde{\rho}\left(\frac{\partial \widetilde{v}_z}{\partial t} + \widetilde{v}_r \frac{\partial \widetilde{v}_z}{\partial r} + \frac{\widetilde{v}_\theta}{r}\frac{\partial \widetilde{v}_z}{\partial \theta} + \widetilde{v}_z \frac{\partial \widetilde{v}_z}{\partial z}\right) = -\frac{\partial \widetilde{p}}{\partial z} \tag{8.38}$$

Assuming small perturbations yields:

$$\frac{\partial p}{\partial r} = -\rho_\infty \frac{\partial v_r}{\partial t} \tag{8.39}$$

$$\frac{\partial p}{\partial z} = -\rho_\infty \frac{\partial v_z}{\partial t} \tag{8.40}$$

If one applies the first boundary condition, which imposes $\frac{\partial v_r}{\partial t} = 0$ at $r = R$ and $\frac{\partial v_z}{\partial t} = 0$ at $z = 0$ and $z = L$, one finds $\frac{\partial p}{\partial r} = \frac{\partial p}{\partial z} = 0$ at those locations. Therefore, the derivatives of $R(r)$ and $Z(z)$ with respect to its own arguments at those locations is also zero.

Referring to the second boundary condition, since the function $p(r, \theta, z, t)$ is always finite, the constant B in equation 8.30 must be zero, as the Bessel function of the second kind $Y_n(r)$ goes to infinite at $r = 0$. Therefore:

$$R(r) = A J_n\left(\frac{\alpha r}{R}\right) \tag{8.41}$$

By taking its derivative with respect to r, and by taking into account the first boundary condition, one finds:

$$J_n'(\alpha) = 0 \tag{8.42}$$

Equation 8.42 has as infinite number of possible solutions α_{mn}', which is the $(m+1)$ root of $J_n'(r)$. For convenience:

$$\pi\alpha_{mn} = \alpha_{mn}' \tag{8.43}$$

Therefore:

$$J_n'(\pi\alpha_{mn}) = 0 \tag{8.44}$$

Table 8.1 – Values of α_{mn}

n \ m	0	1	2	3	4
0	0.000	1.220	2.333	3.238	4.241
1	0.586	1.697	2.717	3.726	4.731
2	0.972	2.135	3.173	4.192	5.204
3	1.337	2.551	3.612	4.643	5.662
4	1.693	2.995	4.037	5.082	6.110

Source: (Zucrow and Hoffman, 1977)

The values for the roots α_{mn} were obtained by (Converse and Hoffman, 1967) and are reproduced in table 8.1, for m and n ranging from 0 to 4. Next, E and F are obtained. By differentiating equation 8.27, one finds:

$$\frac{\partial}{\partial z}[Z(z)] = E\left(i\frac{\xi}{L}\right)\exp\left(i\frac{\xi z}{L}\right) + F\left(-i\frac{\xi}{L}\right)\exp\left(-i\frac{\xi z}{L}\right) \tag{8.45}$$

Imposing that $\frac{\partial Z}{\partial z} = 0$ at $z = 0$ yields:

$$E = F \tag{8.46}$$

Further imposing $\frac{\partial Z}{\partial z} = 0$ at $z = L$ leads to:

$$\exp(i\xi) - \exp(-i\xi) = 2\sinh i\xi = 2i\sin\xi = 0 \tag{8.47}$$

Hence:

$$\xi = \pi q \qquad\qquad (q = 0, 1, 2, ...) \tag{8.48}$$

Substituting the above results into equation 8.27 yields:

$$Z(z) = E\left[\exp\left(\frac{i\pi q z}{L}\right) + \exp\left(\frac{-i\pi q z}{L}\right)\right] \tag{8.49}$$

Which becomes:

$$Z(z) = 2E\cos\frac{\pi q z}{L} = E'\cos\frac{\pi q z}{L} \tag{8.50}$$

The relationship between circular frequency (in Hz) and angular frequency (in rad/s) is given by:

$$\omega = 2\pi f \tag{8.51}$$

The third and last boundary condition imposes the periodicity of the pressure field inside the domain. Therefore, from equation 8.28:

$$\Theta(\theta) = \Theta(\theta + 2\pi k) \qquad\qquad (where \quad k = 0, 1, 2, ...) \tag{8.52}$$

Another condition is that equation 8.36, which defines the relationship between separation constants, must be satisfied for all cases. Therefore, by substituting equations 8.43, 8.48 and 8.51 into it, and by solving for the circular frequency, one obtains:

$$f_{m,n,q} = \frac{a_\infty}{2}\left[\left(\frac{\alpha_{mn}}{R}\right)^2 + \left(\frac{q}{L}\right)^2\right]^{1/2} \tag{8.53}$$

Which are the acoustic oscillation frequencies, for each mode, where m, n and q are denoted as wave numbers (zero or integers). Different combinations of these wave numbers lead to particular acoustic modes: m refers to radial oscillation; n to tangential oscillation; and q to longitudinal oscillation. If two or three of the wave numbers are not null, then it characterizes a combination mode, in contrast to a pure mode.

The acoustical behavior of the combustion chamber can be written as the sum of all possible acoustical modes, since each one of them may co-exist inside the cylindrical cavity, given the superposition principle is applicable to the linear equation 8.15. Meanwhile, the pressure disturbance distribution can be written, after substituting equations 8.26, 8.28, 8.41 and 8.50 into 8.17, as:

$$\begin{aligned} p(r,\theta,z,t) = \sum_{m,n,q} A J_n\left(\frac{\pi\alpha_{mn}r}{R}\right)\left[C\exp(in\theta) + D\exp(-in\theta)\right] \\ \left[E'\cos\left(\frac{\pi q z}{L}\right)\right]\left[G\exp(i\omega t) + H\exp(-i\omega t)\right] \end{aligned} \tag{8.54}$$

Since the acoustic pressure is always a real quantity, the above equation may be rewritten as follows:

$$\begin{aligned} p(r,\theta,z,t) = \sum_{m,n,q}\left[J_n\left(\frac{\pi\alpha_{mn}r}{R}\right)\cos\left(\frac{\pi q z}{L}\right)\right](\bar{A}\cos(n\theta)\cos(\omega t) \\ + \bar{B}\cos(n\theta)\sin(\omega t) + \bar{C}\sin(n\theta)\cos(\omega t) + \bar{D}\sin(n\theta)\sin(\omega t)) \end{aligned} \tag{8.55}$$

Where $\bar{A}$,$\bar{B}$, $\bar{C}$ and $\bar{D}$ are real constants related to the complex ones in equation 8.54. The equation can be further rearranged into:

$$\begin{aligned} p(r,\theta,z,t) = \sum_{m,n,q}\left[J_n\left(\frac{\pi\alpha_{mn}r}{R}\right)\cos\left(\frac{\pi q z}{L}\right)\right][M\cos(n\theta + \omega t - \delta_1) \\ + N\cos(n\theta - \omega t - \delta_2)] \end{aligned} \tag{8.56}$$

Where:

$$\bar{A} = M\cos\delta_1 + N\cos\delta_2 \tag{8.57}$$

$$\bar{B} = M\sin\delta_1 - N\sin\delta_2 \tag{8.58}$$

$$\bar{C} = M\sin\delta_1 + N\sin\delta_2 \tag{8.59}$$

$$\bar{D} = -M\cos\delta_1 + N\cos\delta_2 \tag{8.60}$$

Equation 8.56 reveals that the wave motion inside a closed cylinder cavity is composed by standing longitudinal (q) and radial (m) modes and by two tangential modes (n) that rotate in opposite directions. While longitudinal and radial modes are refrained by the rigid boundaries, the tangential modes are free to travel. Nonetheless, when $M = N$, a standing tangential mode is established, by means of the combination of tangential modes spinning in different directions.

The first spinning tangential mode is proven, historically, to be most harmful inside the combustion chamber of a liquid rocket engine. The hazard is due to increased heat transfer to the walls of the chamber, caused by combustion products travelling unrestrained around its circumference (Bennewitz and Frederick, 2013). Conversely, the longitudinal mode is of less concern: it is the most stable, since the nozzle provides considerable damping and the physical and chemical processes near the injector face are not so sensitive to unsteady motions normal to the face (Anderson and Yang, 1995).

Figure 8.1 – Pressure field of the first three tangential (T) and radial (R) modes inside a cylindrical cavity

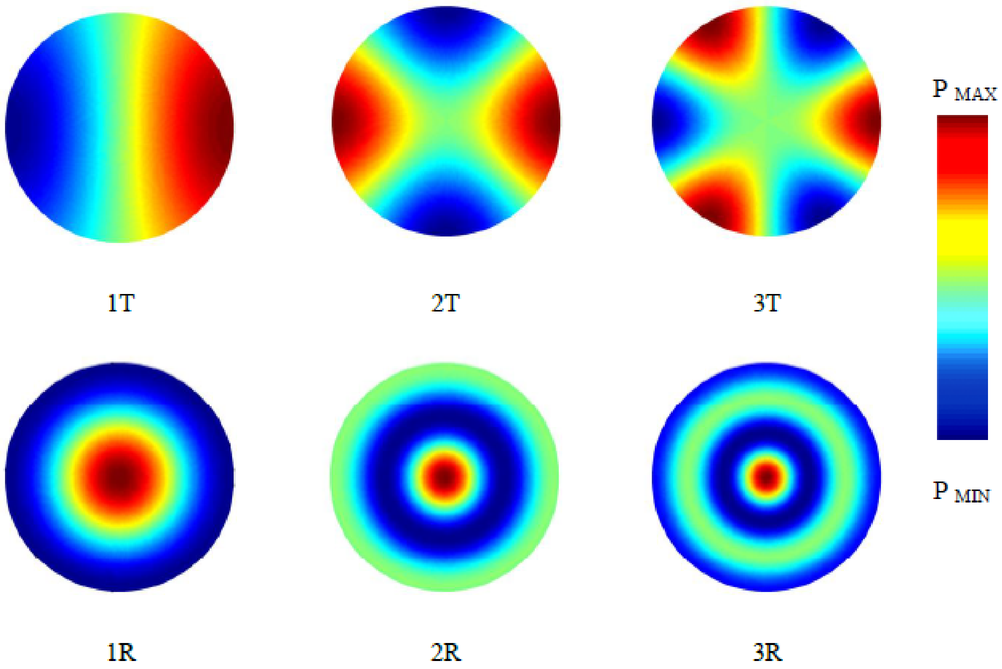

Source: (Losco, d’Agostino, and Paganucci, 2015)

Figure 8.2 – Modes of vibration inside a cylindrical cavity.
(a) Longitudinal mode. (b) Radial mode. (c) Standing tangential mode. (d) Traveling tangential mode

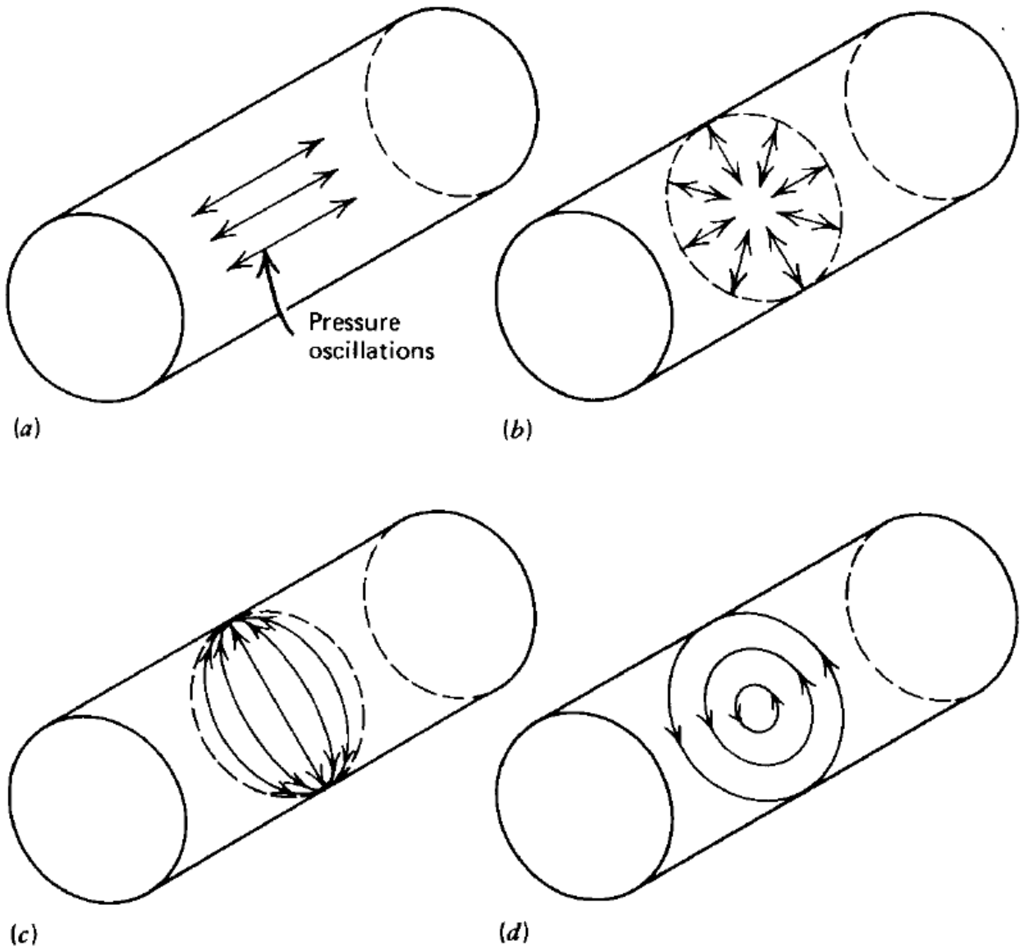

Source: (Zucrow and Hoffman, 1977)

8.3 PASSIVE CONTROL TECHNIQUES

Passive control techniques with regard to combustion instability consist on the installation of physical devices inside the combustion chamber which act in such a manner as to reduce the coupling between combustion processes and acoustic modes or by increasing the inherent damping of the chamber. In the following subsections, two of the most popular elements will be discussed: baffles and acoustic cavities.

8.3.1 BAFFLES

Baffles have been extensively employed as means of preventing combustion instabilities driven by tangential acoustic modes. One of its most notorious uses was on the F-1 engine, which powered the first stage of the Saturn V rocket. After many catastrophic failures at the test stand, a cluster of radial and concentric metal barriers protruding from the face of the injector was envisioned as a way to counteract the unstable pressure waves inside the combustion chamber.

Figure 8.3 – Close-up view of the F-1 injector and detail of the copper baffles

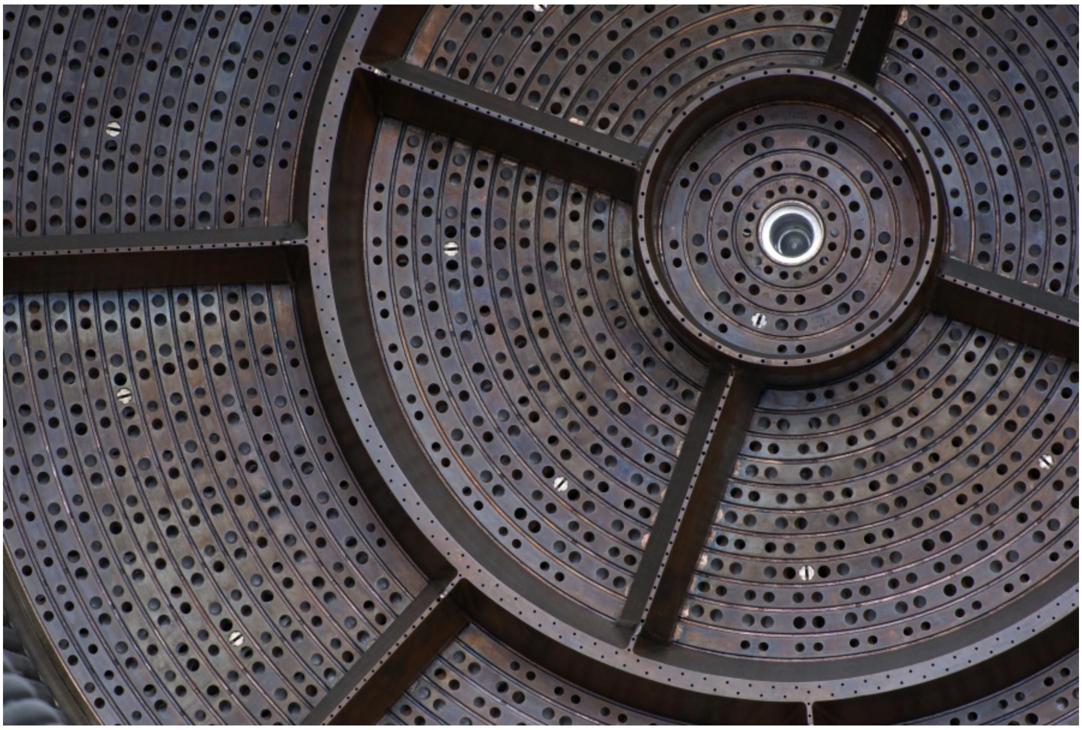

Source: (Jetzer, 2020)

Despite its common use, the mechanisms by which baffles work are not entirely understood (Bennewitz and Frederick, 2013). The proposed theories can be divided into two classes. The first one postulates that baffles reduce the coupling between the combustion processes and the acoustic modes of the engine, by disrupting transverse gas motion or by creating compartments within the chamber with high acoustic frequencies, which results in lower coupling. The second class suggests that baffles increase the damping in the combustion chamber, through the dissipation of oscillatory energy by baffle tip vortices or simply due to drag (Keller, 1974).

Therefore, to this day, most of the development of baffles still rely on a trial-and-error approach. The optimal number and length of baffles for a given configuration, as well as the size of the compartments, are still a subject of study. Some recent work has been developed on the field: (Lubarsky et al., 2008) has investigated the control of combustion instability due to tangential modes by means of an asymmetric baffle, which was gradually inserted on the combustion chamber, to good results (instability was completely suppressed when the baffle was introduced between $10 - 30\%$ of the combustion chamber diameter).

8.3.2 ACOUSTIC CAVITIES

Acoustic cavities are discrete cavities placed near the injector face whose function is to remove oscillatory energy from the combustion chamber, thus providing damping. They are essentially Helmholtz resonators, and therefore they must have a resonant frequency which matches the frequency of the acoustic mode which one wants to dampen.

Figure 8.4 – Model of a resonator. The neck and cavity portions are easily distinguishable

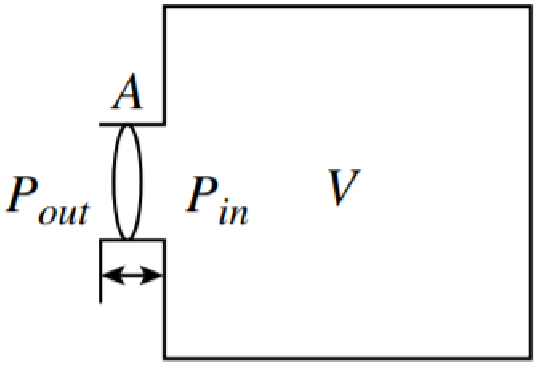

Source: (Kim, 2010)

To find the natural frequency of a Helmholtz resonator, one must find its governing equation, in function of the cavity pressure. In order to derive it, the work by (Kim, 2010) will be used as reference.

First and foremost, the following mathematical formulation is based on the assumption that the volume V of the resonator chamber is much smaller than the cube of the wavelength λ of the disturbance, as follows:

$$V << \lambda^3 \tag{8.61}$$

As such, the entire medium inside the resonator chamber can be said to have constant dynamic characteristics (at a specific point in time) and move in phase.

Once this assumption is made, it can be better understood how the resonator works: once excited by an acoustic wave, the fluid particles on the neck portion of the resonator (which can be treated as one single mass) will compress the fluid particles inside the cavity (which can be treated as a linear spring). Therefore, it can be reasoned that the single mass at the neck will display an oscillatory behaviour, with its kinetic energy being converted to elastic potential energy stored in the cavity, and vice-versa. The energy now inherent to this system was stolen from the acoustic wave, which thus became damped. Maximum damping is achieved when the resonant frequency of the resonator is equal to the frequency of the acoustic wave.

In order to find the governing equation for the pressure inside the cavity, it is logical to relate the time rate of change of pressure to the time rate of change of the volume occupied by the fluid particles sitting inside the cavity. If this changes are small enough, the above relation can be expressed by the following linear equation:

$$\frac{dp}{dt} \propto -\frac{dV}{dt} \tag{8.62}$$

The proportionality symbol can be substituted by the proportional constant C_A, which is called acoustic compliance:

$$C_A \frac{dp}{dt} = -\frac{dV}{dt} \tag{8.63}$$

One can then rewrite the equation for the rate of change of the volume by applying the principle of mass conservation:

$$\frac{dV}{dt} = -Au(t) \tag{8.64}$$

Where A is the cross sectional area of the neck (as seen in Figure 8.4) and $u(t)$ is the velocity of the fluid, also at the neck. This leads to:

$$\frac{dp}{dt} = \frac{1}{C_A} Au(t) \tag{8.65}$$

Considering the fluid motion at the neck and applying Newton's second law yields:

$$p_{out} - p_{in} = \rho_o l \frac{du}{dt} \tag{8.66}$$

Where l is the length of the neck and ρ_o is the density of the fluid particles at the neck. By substituting equation 8.66 into equation 8.65 and making $p_{in} = p$, one can obtain:

$$p + \frac{\rho_o l}{A} \left(C_A \frac{d^2 p}{dt^2} \right) = p_{out} \tag{8.67}$$

Which is the governing equation for the pressure p inside the acoustic cavity, describing its response to an excitation sound pressure p_{out}. It resembles the equation for a vibrating, undamped single degree of freedom system, as expected, and thus its natural frequency is given by:

$$\omega_n = \sqrt{\frac{1}{\frac{\rho_o l}{A} C_A}} \tag{8.68}$$

In order to determine C_A, one must apply the law of conservation of mass, this time to the fluid sitting inside the cavity:

$$\rho_o V = (\rho_o + \Delta\rho)\,(V + \Delta V) \tag{8.69}$$

Neglecting high-order terms leads to:

$$\frac{dV}{dt} = -\frac{V}{\rho_o}\frac{d\rho}{dt} \tag{8.70}$$

Introducing the equation for the speed of sound yields:

$$\frac{dV}{dt} = -\frac{V}{\rho_o {a_\infty}^2}\frac{dp}{dt} \tag{8.71}$$

Finally, by comparing equation 8.71 with equation 8.63 one finds:

$$C_A = \frac{V}{\rho_o {a_\infty}^2} \tag{8.72}$$

And thus:

$$\omega_n = a_\infty\sqrt{\frac{A}{lV}} \tag{8.73}$$

Which is the resonant frequency of a Helmholtz resonator, in rad/s. In Hertz:

$$f_n = \frac{a_\infty}{2\pi}\sqrt{\frac{A}{lV}} \tag{8.74}$$

The length l of the neck is usually substituted by an effective length l', to account for fluid particle around the resonator moving out of phase around the neck. This correction is deemed "end correction", and different relationships are proposed by (Kim, 2010), (Keller, 1974) and (Ginsberg, 2018) (among others), and are usually dependent on the diameter of the neck.

Acoustic cavities are usually placed along the walls of the combustion chamber, for two main reasons: the first one being it is easier to manufacture; the second one is the fact that this is a location where a pressure antinodes exists for all acoustic modes (Sutton and Biblarz, 2016).

8.4 ANALYSES AND RESULTS

Given its aforementioned catastrophic potential, the first spinning tangential mode was chosen as the acoustic mode to suppress inside the combustion chamber of the herein developed liquid rocket engine.

The first step was to find the frequency associated with this mode, by means of equation 8.53, which requires the knowledge of both the the diameter of the combustion chamber and the speed of sound inside it. The combustion chamber diameter D_c was set to 106 mm, after imposing a contraction ratio (combustion chamber cross-sectional area over nozzle throat area) of 6.

The speed of sound was computed as follows:

$$a_\infty = \sqrt{kRT_c} = \sqrt{1.17 \times \frac{8314.46}{24.2} \times 2938.2} = 1\,087\ m/s \tag{8.75}$$

Finally, for the first spinning tangential mode, $m = q = 0$ and $n = 1$, which yielded:

$$f_{m,n,q} = \frac{a_\infty}{2}\left[\left(\frac{\alpha_{mn}}{R}\right)^2 + \left(\frac{q}{L}\right)^2\right]^{1/2} = \frac{a_\infty}{2}\frac{\alpha_{mn}}{R} = \frac{1087}{2}\frac{0.586}{\frac{0.106}{2}} = 6\,009.3\ Hz \tag{8.76}$$

This frequency will also be important for defining the sampling frequency of the pressure transducer on the static test: it should be at least two times higher to comply with the Nyquist−Shannon sampling theorem, if this mode is to be measured.

In order to dampen the first spinning tangential mode, acoustic cavities were chosen over baffles as a passive control device, given their behaviour is currently better understood. The design consists in ten acoustic cavities uniformly distributed around the entire periphery of the combustion chamber, with two of them exhibiting resonant frequencies equal to the one computed above, two having resonant frequencies 5% higher, two having resonant frequencies 5% lower, two having resonant frequencies 10% higher and the last ones having resonant frequencies 10% lower than the nominal one. The ten cavities can be seen in Figure 9.1. This approach aims at dampening the mode even if its frequency reveals itself to be slightly off from the theoretical one, which is expected to happen.

Figure 8.5

– A pair of acoustic cavities is highlighted. The combustion chamber is at the bottom of the figure

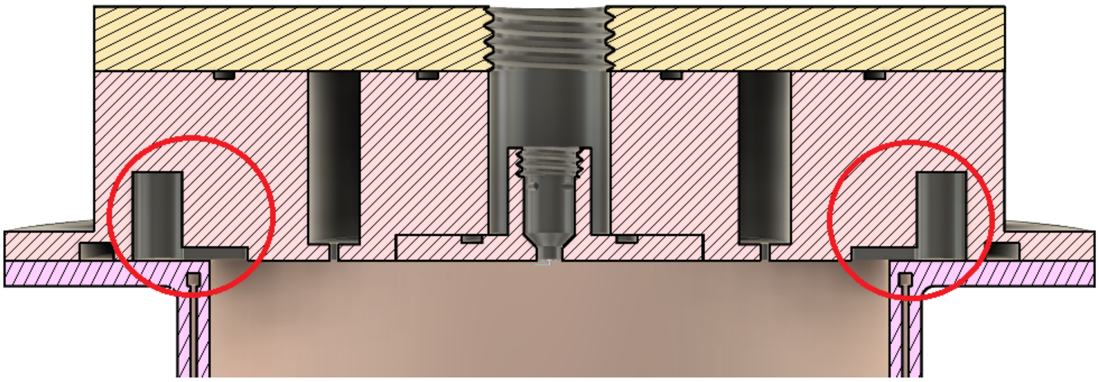

Source: Produced by the authors Ceotto & Tavares

To account for the effective length l' of the resonator, the procedure outlined by (Ginsberg, 2018) was employed:

$$l' = l + 2\left(\frac{8a}{3\pi}\right) \tag{8.77}$$

Where a is the radius of a circle whose area matches that of the rectangular cross section of the neck.

In order to change the resonant frequencies between the pairs of resonators, the length of the cavity was altered. Table 8.2 contains the most important design parameters with respect to the five pairs of resonators.

Table 8.2 – Design parameters of the five pairs of acoustic cavities

Acoustic cavities	1st pair	2nd pair	3rd pair	4th pair	5th pair
Length of neck (mm)	4.0	4.0	4.0	4.0	4.0
Width of neck (mm)	2.0	2.0	2.0	2.0	2.0
Depth of neck (mm)	2.0	2.0	2.0	2.0	2.0
Eff. length of neck (mm)	5.92	5.92	5.92	5.92	5.92
Cavity radius (mm)	4.0	4.0	4.0	4.0	4.0
Cavity length (mm)	11.1	10.1	12.4	9.2	13.8
Resonant frequency (Hz)	6009	6310	5709	6610	5408

The order of magnitude of the volume of the cavities is 10^{-7}, while the order of magnitude of the cube of the wavelength is 10^{-3}, which is in accordance with the assumption presented in equation 8.61.

9 INJECTOR ASSEMBLY AND TEST STAND DESIGN

9.1 INJECTOR ASSEMBLY

A conceptual design for the injector assembly is proposed. The goal was to come up with a model that was easy to assemble and not too challenging to manufacture. Nevertheless, calculations will be carried out in future work in order to verify if this design is suitable under the expected structural and thermal loads.

Ethanol is fed to the injector through the axial port, while nitrous oxide is fed through the lateral one.

Figure 9.1 – CAD render of the injector assembly - Front View

Source: Produced by the authors Ceotto & Tavares

Figure 9.2 – CAD render of the injector assembly - Rear View

Source: Produced by the authors Ceotto & Tavares

Figure 9.3 – Cross-section view of the injector assembled to the combustion chamber

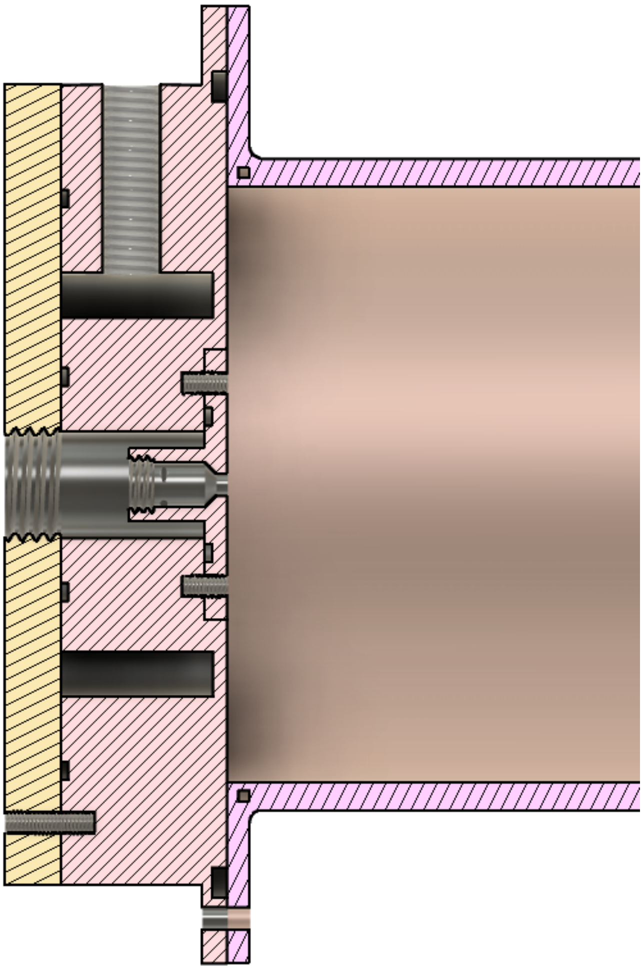

Source: Produced by the authors Ceotto & Tavares

9.2 TEST STAND DESIGN

As the future goal of the present work is to conduct a hot-firing test of the designed liquid rocket engine, significant effort has been made to appropriately plan the experiment.

The focus of this first draft of the hot-firing test bench was determining the main components which needed to be present for testing, the pipping system necessary to connect them, where to place valves, the necessary safety systems, and the desired instrumentation.

In each section of this chapter, each matter is discussed to its own right. However, it is important to emphasize that this is only a first draft of the test bench and shall evolve in every aspect before being fully implemented.

9.2.1 MAIN COMPONENTS

The test bench will support the following 7 main components:

- Oxidizer tank;
- Fuel tank, with refuelling capability;
- Pressurizing gas tank;
- Engine injector;
- Combustion chamber;
- Nozzle;
- Cooling System.

The oxidizer tank shall be a commercial off the shelf (COTS) saturated N_2O tank, self-pressurized to about 60 bar. In order to obtain the necessary oxidizer mass flow ratio during the hot-fire, the liquid N_2O must be consumed. Therefore, this tank will need to be flipped up-side down and fixed accordingly.

The fuel tank, on the other hand, will be a custom designed pressure-vessel manufactured in-house to hold ethanol at 60 bar. After the empty depressurized tank is partially fueled with the desired amount of ethanol before each hot-fire, it will be pressurized again with nitrogen gas.

This nitrogen gas will come from a commercial off the shelf N_2 tank, unmodified to guarantee its safety. Another nitrogen gas tank will also be used as a purging and extinguishing system. This tank will be explained in the safety systems section.

Finally, the last main components are the injector, combustion chamber and nozzle. The nozzle and the combustion chamber shall be equipped with a cooling system, where ethanol will be used to keep both systems and their maximum working temperature before being re-injected for combustion.

9.2.2 SAFETY SYSTEMS

The integrity of the system, the infrastructure and the safety of the researchers carrying out the hot-firing is the main priority during each test.

To certify that every hot-fire can be performed without hazards, it is important to have safety systems in place which prevent accidents from happening as well as act to mitigate problems if the do occur.

The first line of safety that shall be employed is the appropriate evacuation of the room in which the test bench will be located. For this to be possible, many systems will need to be operated remotely. Therefore, the main valves, which control the flow of the oxidizer, the fuel and the purge gas will be solenoid valves operated from a distance. Furthermore, instrumentation shall be digital, also facilitating remote operation.

The second safety system in place are no-return valves which certify that each fluid can only flow in the desired direction, out of the reservoirs.

The third system is the purge gas injection itself. To avoid fuel and oxidizer left-overs after each firing, a purge gas will be used, cleaning up the piping, the injector, the combustion chamber and the nozzle.

The purge system can also be used as a final safety mechanism in case a hazard is created inside the combustion chamber, for example, due to combustion instability or due to material failure. In such case, the purge gas should be released rapidly, extinguishing any flames and cooling down the systems.

9.2.3 INSTRUMENTATION

A detailed planning of the instrumentation will be need to collect the desired data from each hot-firing. For now, a key set of sensors are already known to be useful.

First, pressure and temperature shall be measured along the each line of fluid, which includes the oxidizer line and the fuel line. Furthermore, these sensors are needed right after the fluids leave their tanks and right before they go into the injector.

Flow meters will also be used to determine the volumetric flow rate of the fuel and oxidizer. Combined with data from the pressure and temperature sensors, the mass flow rate of each fluid will be determined.

It is important to not that the type of each sensor has not yet been determined.

9.2.4 EXPERIMENT DIAGRAM

Combining the components of the test bench, together with the safety systems and the instrumentation, a first diagram of the experiment can be formed. It is shown in Figure 9.4.

The piping has been though-out to accommodate the necessary valves and instrumentation, although further analysis of the piping for the cooling system is yet to be performed.

Overall, this first draft of the experiment diagram already contains important details of what the test bench will become. Most importantly, it helps answer questions such as how the experiment will be controlled and performed. Furthermore, it also raises key points that still need to be determined, such as the infrastructure to hold and fix each system and the necessary exhaust evacuation lines.

Figure 9.4 – Piping and instrumentation diagram of hot-firing experiment.

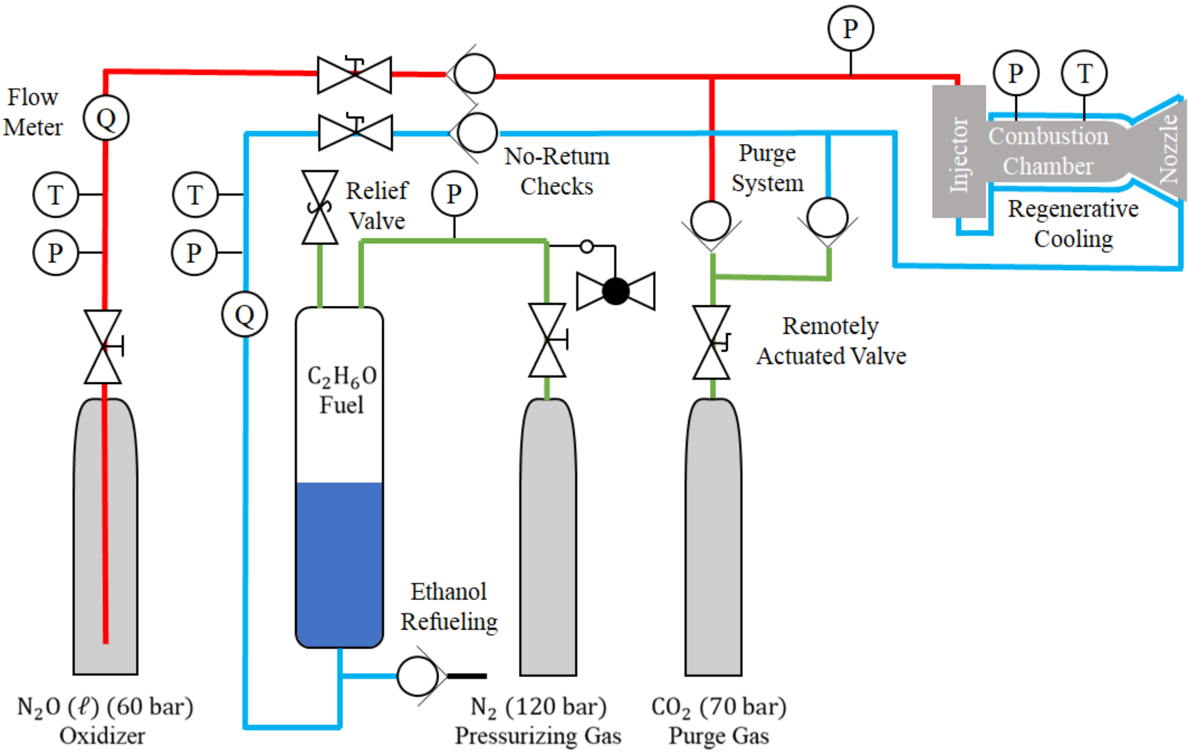

Source: Produced by the authors Ceotto & Tavares

10 CONCLUSION

The main performance parameters of a small-scale rocket engine with ethanol and nitrous oxide as propellants were computed. From these specifications, an analytical analysis was carried out to design both the pressure-swirl ethanol injector and the nitrous oxide plate orifice injector.

For the ethanol injector, results from numerical simulations were confronted with the outputs from the analytical results. The Volume-of-Fluid method showed great agreement with respect to discharge coefficient and film thickness at the exit, while the spray cone half-angle was considerably lower than expected due to viscosity.

Three new mechanisms for ethanol-nitrous oxide combustion were created and confronted against each other, on the basis of ignition delay. Although they showed similar behaviour, the *Marinov + Mevel* model was chosen for the one-dimensional reactor simulation, which allowed to calculate the lifetime of ethanol droplets and the combustion chamber length.

Furthermore, combustion instability was studied, with the frequency for the first spinning tangential acoustic mode (considered to be the most harmful for liquid engine operation) being computed, and acoustic cavities being designed as passive control devices to suppress this mode.

Moreover, a preliminary diagram of the test bench for the rocket engine was developed, along with the conceptual design of the injector assembly.

Future work will be focused on improving the numerical simulations for the ethanol injector and on carrying out cold flow tests (for both of the injectors) and a static fire test.

REFERENCES

Anderson, William E and Vigor Yang. *Liquid rocket engine combustion instability.* American Institute of Aeronautics and Astronautics, 1995.

Ansys, Inc. "ANSYS FLUENT Theory Guide". In: *Canonsburg, Pa* (2020), p. 1026.

Belal, H, Ah El-S Makled, and M A Al-Sanabawy. "Vaporization-controlled simplified model for liquid propellant rocket engine combustion chamber design". In: *IOP Conference Series: Materials Science and Engineering* 610 (Oct. 2019), p. 012088. DOI: `10.1088/1757-899x/610/1/012088`. URL: `https://doi.org/10.1088%2F1757-899x%2F610%2F1%2F012088`.

Bell, Ian H. et al. "Pure and Pseudo-pure Fluid Thermophysical Property Evaluation and the Open-Source Thermophysical Property Library CoolProp". In: *Industrial & Engineering Chemistry Research* 53.6 (2014), pp. 2498–2508. DOI: `10.1021/ie4033999`. eprint: `http://pubs.acs.org/doi/pdf/10.1021/ie4033999`. URL: `http://pubs.acs.org/doi/abs/10.1021/ie4033999`.

Bennewitz, John W and Robert A Frederick. "Overview of combustion instabilities in liquid rocket engines-coupling mechanisms & control techniques". In: *49th AIAA/ASME/SAE/ASEE Joint PropulsionConference*. 2013, p. 4106.

Cancino, L. R. et al. "Measurement and Chemical Kinetics Modeling of Shock-Induced Ignition of EthanolAir Mixtures". In: *Energy & Fuels* 24.5 (2010), pp. 2830–2840. DOI: `10.1021/ef100076w`. eprint: `https://doi.org/10.1021/ef100076w`. URL: `https://doi.org/10.1021/ef100076w`.

Ceotto, G., L. Dias, and G. Tavares. "NOELLE - Development of liquid rocket motors for sounding rockets". In: *GitHub* (2020). DOI: `10.5281/zenodo.4075651`.

Converse, John W and Joe D Hoffman. "Acoustic standing waves in a rocket combustion chamber with ring and spoke baffles". In: (1967).

Dyer, Jonny et al. “Modeling feed system flow physics for self-pressurizing propellants”. In: *43rd AIAA/ASME/SAE/ASEE Joint Propulsion Conference & Exhibit*. 2007, p. 5702.

Gamper, E and R Hink. *Design and test of nitrous oxide injectors for a hybrid rocket engine*. Deutsche Gesellschaft für Luft-und Raumfahrt-Lilienthal-Oberth eV, 2013.

Giffen, Edmund and Alexander Muraszew. *The atomization of liquid fuels*. Chapman & Hall, 1953.

Ginsberg, Jerry H. *Acoustics: A Textbook for Engineers and Physicists*. Vol. 1. Springer, 2018.

Goodwin, David G et al. *Cantera: An Object-oriented Software Toolkit for Chemical Kinetics, Thermodynamics, and Transport Processes*. Version 2.4.0. Aug. 2018. DOI: `10.5281/zenodo.1174508`. URL: `https://doi.org/10.5281/zenodo.1174508`.

Gordon, S. and B. J. McBride. *Computer program for calculation of complex chemical equilibrium compositions and applications. Part 1: Analysis*. Tech. rep. NASA, 1994.

Henry, Robert E and Hans K Fauske. “The two-phase critical flow of one-component mixtures in nozzles, orifices, and short tubes”. In: (1971).

Jetzer, Mike. *F-1 Engine*. Accessed: 2020-11-19. 2020. URL: `http://heroicrelics.org/ussrc/engines-f-1-dcse/dsc80292.jpg.html`.

Kakami, Akira et al. “Plasma-Assisted Combustion of N2O/Ethanol Propellant for Space Propulsion”. In: *46th AIAA/ASME/SAE/ASEE Joint Propulsion Conference - Exhibit*. American Institute of Aeronautics and Astronautics, July 2010. DOI: `10.2514/6.2010-6806`. URL: `https://doi.org/10.2514/6.2010-6806`.

Kang, Zhongtao et al. “Review on pressure swirl injector in liquid rocket engine”. In: *Acta Astronautica* 145 (2018), pp. 174–198.

Keller, Russell B. *Liquid rocket engine combustion stabilization devices*. National Aeronautics and Space Administration, 1974.

Kim, Yang-Hann. *Sound propagation: an impedance based approach*. John Wiley & Sons, 2010.

Lee, Inchul, Min Son, and Jaye Koo. “Atomization and Combustion Characteristics of Ethanol/Nitrous Oxide at Various Momentum Flux Ratios”. In: *Energy & Fuels* 28.4 (2014), pp. 2770–2779. DOI: `10.1021/ef402251s`. eprint: `https://doi.org/10.1021/ef402251s`. URL: `https://doi.org/10.1021/ef402251s`.

Lefebvre, Arthur H and Vincent G McDonell. *Atomization and sprays*. CRC press, 2017.

Losco, Pio Luciano, Luca d’Agostino, and Fabrizio Paganucci. “Analysis of the first tangential mode in a cylindrical rocket engine combustion chamber equipped with an absorber”. In: (2015).

Lubarsky, Eugene et al. “Control of Tangential Combustion Instability by Asymmetric Baffle”. In: *46th AIAA Aerospace Sciences Meeting and Exhibit*. 2008, p. 955.

Lyras, Konstantinos et al. “Numerical simulation of subcooled and superheated jets under thermodynamic non-equilibrium”. In: *International Journal of Multiphase Flow* 102 (2018), pp. 16–28.

Maly, Milan, Jan Jedelsky, et al. “Internal flow and air core dynamics in Simplex and Spill-return pressure-swirl atomizers”. In: *International Journal of Heat and Mass Transfer* 123 (2018), pp. 805–814.

Maly, Milan, Jaroslav Slama, et al. “2D and 3D numerical modelling of internal flow of Pressure-swirl atomizer”. In: *EPJ Web of Conferences*. Vol. 213. EDP Sciences. 2019, p. 02055.

Marinov, Nick M. “A detailed chemical kinetic model for high temperature ethanol oxidation”. In: *International Journal of Chemical Kinetics* 31.3 (1999), pp. 183–220. DOI: `https://doi.org/10.1002/(SICI)1097-4601(1999)31:3<183::AID-KIN3>3.0.CO;2-X`. eprint: `https://onlinelibrary.wiley.com/doi/pdf/10.1002/%28SICI%291097-4601%281999%2931%3A3%3C183%3A%3AAID-KIN3%3E3.0.CO%3B2-X`. URL: `https://onlinelibrary.wiley.com/doi/abs/10.1002/%28SICI%291097-4601%281999%2931%3A3%3C183%3A%3AAID-KIN3%3E3.0.CO%3B2-X`.

Mével, R. et al. “Hydrogennitrous oxide delay times: Shock tube experimental study and kinetic modelling”. In: *Proceedings of the Combustion Institute* 32.1 (2009), pp. 359–366. ISSN: 1540-7489. DOI: `https://doi.org/10.1016/j.proci.2008.06.171`. URL: `http://www.sciencedirect.com/science/article/pii/S1540748908003180`.

MONAT, J. P., R. K. HANSON, and C. H. KRUGER. "Kinetics of Nitrous Oxide Decomposition". In: *Combustion Science and Technology* 16.1-2 (1977), pp. 21–28. DOI: `10.1080/00102207708946790`. eprint: `https://doi.org/10.1080/00102207708946790`. URL: `https://doi.org/10.1080/00102207708946790`.

Palacz, Tomasz. "Nitrous Oxide Application for Low-Thrust and Low-Cost Liquid Rocket Engine". In: (2017). DOI: `10.13009/EUCASS2017-474`. URL: `https://www.eucass.eu/doi/EUCASS2017-474.pdf`.

Phillip, Jeff et al. "Development and testing of a nitrous-oxide/ethanol bi-propellant rocket engine". In: *52nd AIAA/SAE/ASEE Joint Propulsion Conference*. American Institute of Aeronautics and Astronautics, July 2016. DOI: `10.2514/6.2016-5092`. URL: `https://doi.org/10.2514/6.2016-5092`.

Rayleigh, John William Strutt Baron. *The theory of sound*. Vol. 2. Macmillan, 1896.

Saxena, Priyank and Forman A. Williams. "Numerical and experimental studies of ethanol flames". In: *Proceedings of the Combustion Institute* 31.1 (2007), pp. 1149–1156. ISSN: 1540-7489. DOI: `https://doi.org/10.1016/j.proci.2006.08.097`. URL: `http://www.sciencedirect.com/science/article/pii/S1540748906003609`.

Sher, Eran, Tali Bar-Kohany, and A. Rashkovan. "Flash-boiling atomization". In: *Progress in Energy and Combustion Science* 34 (Aug. 2008), pp. 417–439. DOI: `10.1016/j.pecs.2007.05.001`.

Smith, Gregory P. et al. *GRI-Mech 3.0*. Accessed: 2020-11-19. 2000. URL: `http://combustion.berkeley.edu/gri-mech/version30/text30.html`.

Solomon, Brian J. "Engineering Model to Calculate Mass Flow Rate of a Two-Phase Saturated Fluid Through An Injector Orifice". In: (2011).

Spalding, D. B. "Combustion in Liquid-Fuel Rocket Motors". In: *Aeronautical Quarterly* 10.1 (1959), pp. 1–27. DOI: `10.1017/S0001925900001402`.

Sun, Yubiao et al. "Numerical and experimental study on the spray characteristics of full-cone pressure swirl atomizers". In: *Energy* 160 (2018), pp. 678–692.

Sutton, George P and Oscar Biblarz. *Rocket propulsion elements*. John Wiley & Sons, 2016.

Tokudome, Shinichiro et al. "Experimental Study of an N2O/Ethanol Propulsion System". In: *43rd AIAA/ASME/SAE/ASEE Joint Propulsion Conference - Exhibit*. American Institute of Aeronautics and Astronautics, July 2007. DOI: `10.2514/6.2007-5464`. URL: `https://doi.org/10.2514/6.2007-5464`.

Turns, Stephen R. *An Introduction to Combustion: Concepts and Applications*. McGraw-Hill, 1996.

Wang, Lu-Qing, Hong-Hao Ma, and Zhao-Wu Shen. "Explosion characteristics of H2/N2O and CH4/N2O diluted with N2". In: *Fuel* 260 (2020), p. 116355. ISSN: 0016-2361. DOI: `https://doi.org/10.1016/j.fuel.2019.116355`. URL: `http://www.sciencedirect.com/science/article/pii/S0016236119317090`.

Waxman, Benjamin S et al. "Mass flow rate and isolation characteristics of injectors for use with self-pressurizing oxidizers in hybrid rockets". In: *49th AIAA/ASME/SAE/ASEE Joint PropulsionConference*. 2013, p. 3636.

Whitmore, Stephen A. and Spencer N. Chandler. "Engineering Model for Self-Pressurizing Saturated-N2O-Propellant Feed Systems". In: *Journal of Propulsion and Power* 26.4 (2010), pp. 706–714. DOI: `10.2514/1.47131`.

Xue, J et al. "Effect of geometric parameters on simplex atomizer performance". In: *AIAA journal* 42.12 (2004), pp. 2408–2415.

Zucrow, Maurice Joseph and Joe D Hoffman. "Gas dynamics. Volume 2-Multidimensional flow". In: *nyjw* (1977).